The SAURON project – II. Sample and early results

P. Tim de Zeeuw,[1]⋆ M. Bureau,[1] Eric Emsellem,[2] R. Bacon,[2] C. Marcella Carollo,[3]
Y. Copin,[1,2] Roger L. Davies,[4] Harald Kuntschner,[4] Bryan W. Miller,[5] G. Monnet,[6]
Reynier F. Peletier[7] and E. K. Verolme[1]

[1]*Sterrewacht Leiden, Niels Bohrweg 2, 2333 CA, Leiden, the Netherlands*
[2]*CRAL-Observatoire, 9 Avenue Charles–André, 69230 Saint-Genis-Laval, France*
[3]*Department of Astronomy, Columbia University, 538 West 120th Street, New York, NY 10027, USA*
[4]*Physics Department, University of Durham, South Road, Durham DH1 3LE*
[5]*Gemini Observatory, Casilla 603, La Serena, Chile*
[6]*European Southern Observatory, Karl-Schwarzschild Strasse 2, D-85748 Garching, Germany*
[7]*Department of Physics and Astronomy, University of Nottingham, University Park, Nottingham NG7 2RD*

ABSTRACT

Early results are reported from the SAURON survey of the kinematics and stellar populations of a representative sample of nearby E, S0 and Sa galaxies. The survey is aimed at determining the intrinsic shape of the galaxies, their orbital structure, the mass-to-light ratio as a function of radius, the age and metallicity of the stellar populations, and the frequency of kinematically decoupled cores and nuclear black holes. The construction of the representative sample is described, and its properties are illustrated. A comparison with long-slit spectroscopic data establishes that the SAURON measurements are comparable to, or better than, the highest-quality determinations. Comparisons are presented for NGC 3384 and 4365, where stellar velocities and velocity dispersions are determined to a precision of $6\,\mathrm{km\,s^{-1}}$, and the h_3 and h_4 parameters of the line-of-sight velocity distribution to a precision of better than 0.02. Extraction of accurate gas emission-line intensities, velocities and linewidths from the data cubes is illustrated for NGC 5813. Comparisons with published line strengths for NGC 3384 and 5813 reveal uncertainties of $\lesssim 0.1\,\text{Å}$ on the measurements of the Hβ, Mg b and Fe5270 indices. Integral-field mapping uniquely connects measurements of the kinematics and stellar populations to the galaxy morphology. The maps presented here illustrate the rich stellar kinematics, gaseous kinematics, and line-strength distributions of early-type galaxies. The results include the discovery of a thin, edge-on, disc in NGC 3623, confirm the axisymmetric shape of the central region of M32, illustrate the LINER nucleus and surrounding counter-rotating star-forming ring in NGC 7742, and suggest a uniform stellar population in the decoupled core galaxy NGC 5813.

Key words: galaxies: elliptical and lenticular, cD – galaxies: kinematics and dynamics – galaxies: spiral – galaxies: stellar content.

1 INTRODUCTION

The physical properties of early-type galaxies correlate with luminosity and environment. The morphology–density relation (Dressler 1980) shows that elliptical and lenticular galaxies are much more common in clusters than they are in regions of lower local density. Giant ellipticals are red, have a high metal content, often have boxy isophotes, are supported by anisotropic velocity distributions and have triaxial figures (e.g. de Zeeuw & Franx 1991), whereas lower-luminosity systems are bluer, less metal-rich, have discy isophotes, are flattened by rotation, and may well have nearly oblate shapes (Davies et al. 1983; Bender & Nieto 1990; de Zeeuw & Carollo 1996; Faber et al. 1997).

Observations with the *Hubble Space Telescope* have re-enforced the connection between the global and core properties of early-type galaxies. The nuclei of elliptical and lenticular galaxies, as well as the bulges of early-type spirals, often contain stellar and/or gaseous discs, possibly associated with a massive central black hole, as well as unresolved nuclear spikes, kinematically decoupled structures, and puzzling asymmetries. These *nuclear* properties loosely

⋆E-mail: tim@strw.leidenuniv.nl

correlate with the *global* structure of the galaxies. For example, while the luminosity profiles of elliptical galaxies approach a power-law $\rho(r) \propto r^{-\gamma}$ at small radii r, giant ellipticals ($M_B < -20.5$) have *shallow* cusps (mean $\gamma \approx 0.8$) and low-luminosity ellipticals ($M_B > -20.5$) have *steep* cusps (mean $\gamma \approx 1.9$) (Jaffe et al. 1994; Faber et al. 1997). At intermediate luminosities, both types of profile occur (Carollo et al. 1997; Rest et al. 2001). Furthermore, it appears that the mass of the central black hole correlates with the velocity dispersion of the host galaxy (Ferrarese & Merritt 2000; Gebhardt et al. 2000b).

At present, it is unclear to what extent the observed properties of these early-type galaxies, and the correlations between them, were acquired at the epoch of galaxy formation or result from subsequent dynamical evolution, possibly driven by a central black hole (Franx, Illingworth & de Zeeuw 1991; de Zeeuw 1996; Faber et al. 1997; Merritt 1999; Bak & Statler 2000). Key questions in this area include: what is the distribution of intrinsic shapes, tumbling speeds, and internal orbital structure of early-type galaxies? How do these depend on total luminosity and environment? What is the shape and extent of the dark halo? What is the dynamical importance of the central black hole? What is the distribution of metals, and what is the relation between the kinematics of stars (and gas), the local metal enrichment, and the star formation history?

Progress towards answering these questions requires a systematic investigation of the kinematics and line strengths of a representative sample of early-type systems. The intrinsic shape, internal orbital structure and radial dependence of the mass-to-light ratio M/L are constrained by the line-of-sight velocity distribution of the stars (e.g. van der Marel & Franx 1993; Gerhard 1993) and by the gas kinematics (e.g. Cretton, Rix & de Zeeuw 2000). The absorption line strengths can be used to infer the luminosity-weighted age and metallicity of the stellar populations (Carollo, Danziger & Buson 1993; Davies, Sadler & Peletier 1993; González 1993; Worthey 1994). Detailed studies of individual galaxies are valuable, but need to be complemented with a systematic investigation of the internal structure as a function of global properties, such as total luminosity and Hubble type, and environment.

Studies of the kinematics and line-strength distributions of galaxies have traditionally relied on long-slit spectroscopy along at most a few position angles (e.g. Davies & Birkinshaw 1988; Franx, Illingworth & Heckman 1989; Bender, Saglia & Gerhard 1994; Surma & Bender 1995; Statler & Smecker-Hane 1999). This is insufficient to map the rich internal structure of early-type galaxies (Statler 1991, 1994; Arnold, de Zeeuw & Hunter 1994). Constructing full two-dimensional maps for a significant sample of galaxies with long-slit spectroscopy requires a prohibitive amount of telescope time. For this reason, we built SAURON, a panoramic integral-field spectrograph optimized for studies of the large-scale kinematics and stellar populations of galaxies (Bacon et al. 2001, hereafter Paper I). SAURON is based on the same principles as the prototype integral-field spectrograph TIGER, built for the Canada–France–Hawaii Telesope (CFHT), and its successor OASIS (Bacon et al. 1995, 2000). In its low-resolution (LR) mode, SAURON has a 33×41 arcsec field-of-view sampled with 0.94×0.94 arcsec pixels, 100 per cent coverage, high throughput, and a spectral resolution of 3.6 Å fullwidth at half-maximum (FWHM). In high-resolution (HR) mode, the spectral resolution is 2.8 Å and the field of view is 9×11 arcsec, sampled at 0.27×0.27 arcsec. SAURON provides 1577 spectra in one exposure (wavelength range 4810–5350 Å, see also Section 5.3),

146 of which are used for simultaneous sky subtraction 1.9 arcmin away from the main field. Stellar kinematical information is derived from the Mg b triplet and the Fe lines. The [O III] and Hβ emission lines allow derivation of the morphology and kinematics of the ionized gas, and provide information on its ionization state. The Mg b, Hβ, and Fe5270 absorption lines are sensitive to the age and metallicity of the stellar populations. Paper I describes the design and construction of SAURON, and the extensive data reduction software developed. SAURON was commissioned on the William Herschel Telescope (WHT) in 1999 February (de Zeeuw et al. 2000).

We are using SAURON on the WHT to observe a representative sample of nearby ellipticals, lenticulars and early-type spiral bulges, as well as some objects with known peculiar kinematics (e.g. Davies et al. 2001). We will combine the SAURON observations with high spatial resolution spectroscopy of the nuclei, and interpret them using dynamical and stellar population modelling. Here we present selected observations which serve to establish the scientific integrity of the spectrograph, and provide early results from our systematic survey. Section 2 describes the definition of the sample. Section 3 presents stellar kinematic measurements showing evidence for embedded discs and decoupled cores. Section 4 is devoted to measurements of the kinematics and line ratios of extended emission-line gas, and Section 5 presents absorption line-strength measurements. In each of these three sections, we compare the SAURON results with previous long-slit measurements, and show that SAURON is efficient and accurate. Section 6 summarizes the results and outlines the next steps.

2   THE SAURON SAMPLE

Observing any complete sample which spans a wide range of global properties is costly in telescope time, even with SAURON. We have therefore constructed a *representative* sample of nearby early-type galaxies, as free of biases as possible while ensuring the existence of complementary data.

2.1   Selection

We first compiled a complete list of elliptical galaxies, lenticular galaxies and spiral bulges for which SAURON can measure the stellar kinematics. Given the specifications of the instrument when mounted on the WHT (Paper I), this leads to the following constraints: $-6° \leq \delta \leq 64°$ (to limit the zenith distance and therefore the instrumental flexure), $cz \leq 3000 \, \text{km s}^{-1}$ (to ensure that all the lines of interest are in the spectral band), and $M_B \leq -18$ (so that $\sigma \gtrsim 75 \, \text{km s}^{-1}$ and velocity dispersions can be measured). We further restricted the objects to $|b| \gtrsim 15°$ to avoid crowded fields and large Galactic extinctions. All parameters except M_B were taken from the Lyon/Meudon Extragalactic Database (LEDA; see Paturel et al. 1997) and checked for consistency with the RC3 (de Vaucouleurs et al. 1991) through VizieR (Ochsenbein, Bauer & Marcout 2000).

We derived absolute magnitudes following the prescription in LEDA, using the listed heliocentric velocities and apparent magnitudes. We adopted a Virgocentric flow model with $v_{\text{virgo}} = 170 \, \text{km s}^{-1}$, $H_0 = 75 \, \text{km s}^{-1}$, and the correction to the Local Group centroid of Yahil, Tammann & Sandage (1977). For galaxies in the Virgo cluster, the Coma I cloud and the Leo I group, which we refer to as 'cluster' galaxies, we adopted common distances based on the mean heliocentric velocity of each group,
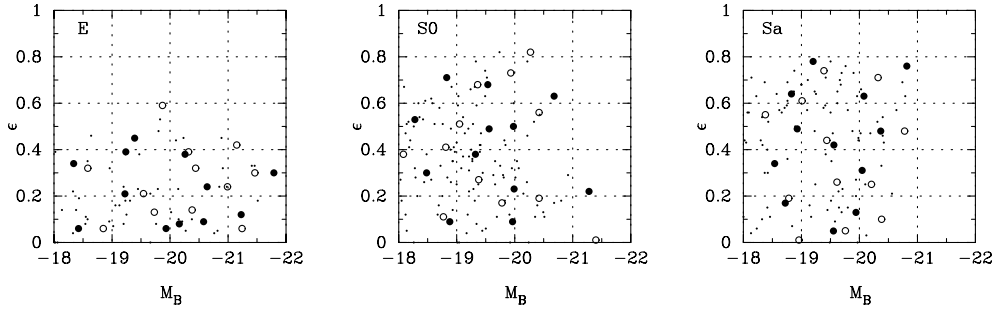
Figure 1. Distribution of 72 E, S0, and Sa galaxies in the SAURON representative sample, in the plane of ellipticity ϵ versus absolute blue magnitude M_B. Filled circles: galaxies in the Virgo cluster, or the Leo and Coma I groups ('cluster' objects). Open circles: other galaxies ('field' objects). Small dots: non-selected 255 galaxies of the complete sample.

taken from Mould et al. (1993). The distances derived, 16.3, 13.7 and 10.7 Mpc (31.04, 30.68 and 30.14 mag), respectively, are in good agreement with those derived from other measurements (see, e.g. Ferrarese et al. 2000). For galaxies outside these three associations, which we refer to as 'field' galaxies, we used individual distances. We took cluster and group membership primarily from Tully (1988) and Garcia (1993), but also from other sources (e.g. Turner & Gott 1976; Huchra & Geller 1982; Geller & Huchra 1983; Faber et al. 1989).

The list of galaxies obtained with the above criteria contains 327 objects. We divided these into six categories by first separating 'cluster' and 'field' galaxies, and then splitting each of these groups into E, S0, and Sa galaxies, based on LEDA's morphological type (E: $T \leqslant -3.0$, S0: $-3.0 < T \leqslant -0.5$, Sa: $-0.5 < T \leqslant 1.5$). This results in 29 E, 51 S0 and 37 Sa galaxies in the 'cluster' environment, and 47 E, 86 S0 and 77 Sa galaxies in the 'field'. We selected a *representative* sample of objects from this complete list by populating the six ellipticity versus absolute magnitude planes nearly uniformly, using bins of 1 mag in luminosity and 0.2 in ellipticity (where ϵ is derived from the axial ratio at the $25 \, \mathrm{mag}^{-2}$ level in B, as reported in LEDA; for the spirals it effectively gives the inclination of the disc). This choice of bin size is appropriate given the range of absolute magnitude we want to cover, and the radial ellipticity variations observed in early-type galaxies. The result is 36 'cluster' galaxies (12 E, 12 S0 and 12

Sa) and 36 'field' galaxies (12 E, 12 S0 and 12 Sa), as illustrated in Fig. 1. A sample of this size is large enough to be sub-divided by morphology, environment and luminosity, yet small enough that complete mapping with SAURON is possible. The 72 galaxies correspond to 22 per cent of the complete sample and, as can be seen from Fig. 1, remain representative of it. Tables A1 and A2 list the 72 galaxies and summarize some of their properties.

Fig. 2 compares distances and absolute luminosities for the 38 sample galaxies in common with the *I*-band surface brightness fluctuation (SBF) survey of Tonry et al. (2001). $\bar{N}_I$ is a distance-independent measure of absolute luminosity. Our distances are in very good agreement with the SBF distances ($\langle |\Delta m_{\mathrm{SBF}} - \Delta m_{\mathrm{VCF}}| \rangle = 0.13$), and our M_B correlates strongly with $\bar{N}_I$. Only seven galaxies have distances differing by more than 0.5 mag (half a bin) from the mean offset. Despite a simplistic approach, our distance estimates are thus accurate enough for the chosen bin size.

The complete list of galaxies is unbiased, but we did consider additional criteria when selecting the representative sample. In cases where more than one galaxy could be used to fill a given bin, we favoured the one for which high spatial resolution imaging and kinematics are available, primarily *Hubble Space Telescope* (*HST*) WFPC2 and STIS observations from the *HST* archive. Such observations are essential to constrain the mass distribution in the nuclei of the galaxies. Similarly, we preferentially chose galaxies
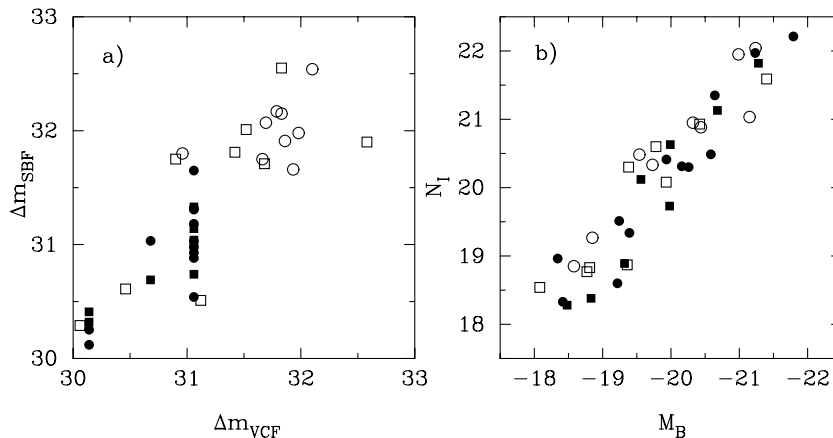

Figure 2. Comparison of distances and absolute luminosities for the galaxies in the SAURON sample for which surface-brightness-fluctuation measurements were reported by Tonry et al. (2001). (a) SBF distance moduli Δm_{SBF} versus Virgocentric distance moduli Δm_{VCF}. (b) SBF fluctuation star counts $\bar{N}_I$ versus absolute magnitudes M_B. Circles: elliptical galaxies. Squares: lenticular galaxies. Filled symbols: 'cluster' objects. Open symbols: 'field' objects. No spiral galaxies are in common between the two sets.

for which kinematics at large radii is available, for example through long-slit spectroscopy or H I observations. These data can be used to evaluate the importance of dark matter in the outer parts of the galaxies. In the case of S0 and Sa galaxies, we also tried to obtain a representative mix of barred and unbarred systems. These choices introduce a bias in the selection, but this bias is hard to quantify. The ground-based observations were primarily compiled using the Hypercat catalogue (e.g. Prugniel et al. 1997) and derive from a range of programs with different goals, but a large fraction of them were carried out as part of statistically complete surveys. Thus, overall, we believe that the bias introduced is minimal, and that the advantages of working with a carefully crafted sample far outweigh the disadvantages.

2.2 Properties of the sample galaxies

Fig. 3 illustrates that the galaxies in our representative sample cover a large range of global and nuclear properties (listed in Tables A1 and A2). Panel (a) presents the Faber–Jackson (Faber & Jackson 1976) relation between total luminosity (absolute blue magnitude M_B; see Section 2.1) and central velocity dispersion σ (LEDA). The galaxies cover a range of ≈ 50 in luminosity and a factor of five in velocity dispersion. Panel (b) plots the effective $B - V$ colour (LEDA) versus σ, and panel (c) plots the central value of Mg_2 (Hypercat) versus σ. These panels demonstrate that large galaxies are systematically redder and have stronger lines. Panel (d) shows the ellipticity-normalized anisotropy parameter $(V/\sigma)^*$ (i.e. V_{max}/σ divided by the value $\sqrt{\epsilon/1-\epsilon}$ for the oblate isotropic rotator of the same ellipticity as the galaxy, where V_{max} is the maximum of the observed stellar mean streaming velocity, see Davies et al. 1983), plotted against the central velocity dispersion for the elliptical galaxies (LEDA). The ellipticities used are those from column 10 of Tables A1 and A2, and are not necessarily

applicable to the domain of the galaxy where the stellar rotation velocity was measured. The values for V_{max} are the averages of the maximum stellar V measured along the major axis for sources listed in LEDA (column 12 of Tables A1 and A2). Upper limits are included as measurements. Discrepancies in the catalogue entries were resolved by examining the original data. The elliptical galaxies in the sample span a wide range of anisotropy. About two dozen galaxies have well-determined nuclear surface brightness profiles derived from *HST* imaging (Lauer et al. 1995; Byun et al. 1996; Carollo et al. 1997; Rest et al. 2001). Panel (e) shows the average logarithmic slope γ_{phys}^V of the deprojected luminosity profile within $10-50$ pc, as derived by Carollo et al. (1997, tables 5 and 8) for 12 of our objects. They display a significant scatter, but lower-dispersion galaxies generally have steeper central cusps. A similar number of objects in our sample also have published values for the mass of a central black hole, based on high-resolution absorption or emission-line spectroscopy and (in most cases) axisymmetric three-integral dynamical modelling (Bower et al. 1998, 2001; Gebhardt et al. 2000a,b; Macchetto et al. 1997; Sarzi et al. 2001). As Panel (f) shows, they cover three orders of magnitude in black hole mass.

3 STELLAR KINEMATICS

Our strategy is to map galaxies out to one effective radius R_e, which for nearly half the sample requires only one SAURON pointing. For large galaxies, mosaics of two or three pointings reach $0.5R_e$, except for M84 and M87 where two additional pairs of flanking fields are needed to reach this minimum radius. Each 2-hr pointing is typically split into four exposures of 1800 s each, dithered by one lenslet. We reduce and merge the raw SAURON exposures as described in Paper I, and use the individual wavelength-calibrated and extracted spectra to derive maps of the stellar kinematics using
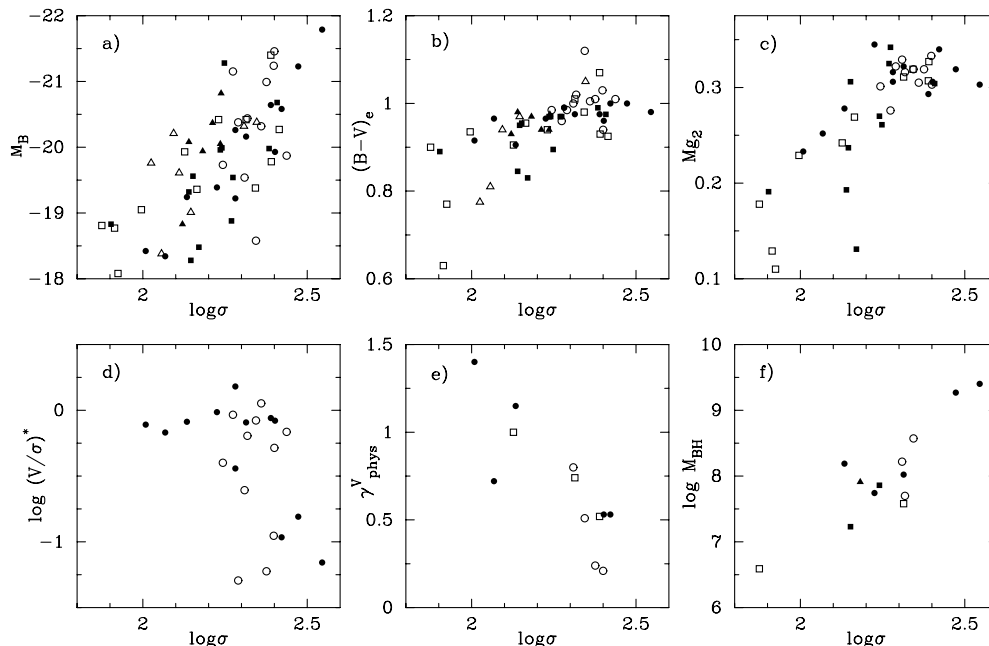

Figure 3. Properties of the galaxies in the SAURON representative sample. Circles: elliptical galaxies. Squares: lenticular galaxies. Triangles: early-type spiral bulges. Filled symbols: 'cluster' objects. Open symbols: 'field' objects. Plotted versus central velocity dispersion σ are (a) absolute blue magnitude M_B, (b) effective $B - V$ colour, (c) central Mg_2 line-strength, (d) measure of rotational support $(V/\sigma)^*$, (e) central cusp-slope γ_{phys}^V of the surface-brightness profile and (f) black hole mass M_{BH}. The data are taken from the literature (see text, and Tables A1 and A2) and error bars are not shown. Most quantities are not available for all galaxies.

the Fourier Correlation Quotient (FCQ) method (Bender 1990) and an optimal stellar template (Paper I, section 5.2). This provides the mean stellar velocity *V* and the velocity dispersion σ, as well as the Gauss–Hermite moments h_3 and h_4, which quantify the first-order asymmetric and symmetric deviations of the line-of-sight velocity distribution from a Gaussian form (van der Marel & Franx 1993; Gerhard 1993).

We estimated the errors on the kinematic parameters by means of extensive Monte Carlo tests: for each galaxy spectrum and its associated set of kinematic parameters, an initial noise-free galaxy spectrum was estimated by convolving the template spectrum with the corresponding analytic line-of-sight velocity distribution. Extraction of a new set of parameters after inclusion of a realization of the noise at the given signal-to-noise ratio constitutes a random realization out of the statistical distribution of these parameters, and the errors on the kinematic parameters are estimated from the variance of 100 realizations of this distribution.

SAURON observations of the kinematics of stars and gas in the E6 galaxy NGC 3377 were presented in fig. 12 of Paper I. Kinematic and line-strength maps of NGC 4365 were published by Davies et al. (2001). In this section we present the SAURON kinematics of NGC 3384 observed with the LR mode, and compare the results with high-quality long-slit kinematics from the literature. We then discuss NGC 3623 and 4365, both of which display significant structure in the observed kinematics which is not captured by long-slit spectroscopy along a few position angles.

We conclude by presenting kinematic maps of M32 taken with the HR mode.

3.1 LR mode observations of NGC 3384

NGC 3384 is a large early-type spiral in the Leo I group, classified as SB0$^-$(s) in the RC3 ($M_B = -19.56$, $T = -2.6$ in LEDA). It forms a triple on the sky with NGC 3379 and 3389, but there is only marginal evidence for interactions in the form of a faint spiral or tidal arm (Malin 1984) and the existence of a large H I ring around the triple (Schneider 1985). Barbon, Capaccioli & Tarenghi (1975) described the three main components of NGC 3384: a bright $R^{1/4}$ central region ($r \lesssim 20$ arcsec), a lens ($r \lesssim 160$ arcsec), and an outer exponential disc ($r \gtrsim 160$ arcsec). The light distribution in the central ≈ 20 arcsec is complex. The inner isophotes are elongated along the major axis, suggesting an embedded disc, but beyond 10 arcsec the elongation is along the minor-axis, possibly due to a faint polar ring or bar (Davoust et al. 1984; Whitmore et al. 1990; Busarello et al. 1996). At much larger radii the isophotes are off-centred. NGC 3384 shows no emission lines (Ho, Filippenko & Sargent 1997), remains undetected in H I, CO, radio continuum, and X-ray (e.g. Roberts et al. 1991), but has *IRAS* 12- and 100-μm fluxes (Knapp et al. 1989).

We observed NGC 3384 with SAURON in LR mode on the night of 2000 April 4. We obtained 4×1800 s on one field centred on the galaxy, which covers most of the bulge. The seeing was 2.5 arcsec.
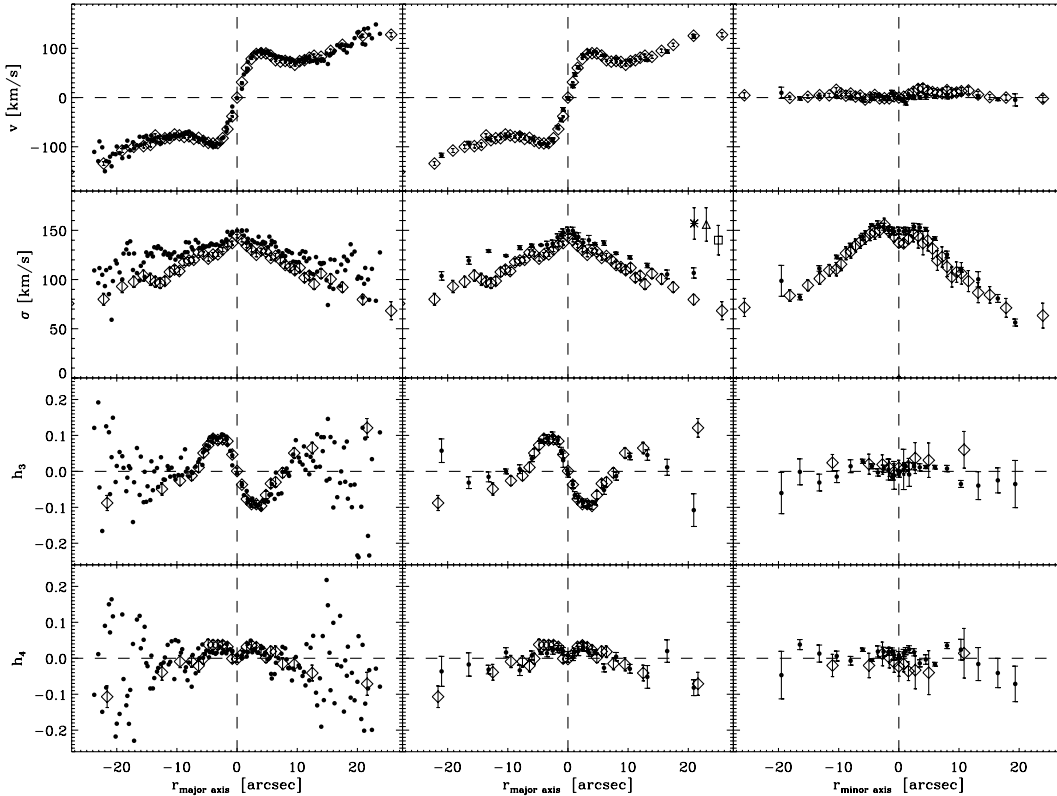

Figure 5. Comparison of the SAURON kinematics of NGC 3384 (dots) with the long-slit measurements of Fisher (1997, diamonds, 2 arcsec slit). Top to bottom: mean velocity *V*, velocity dispersion σ, and Gauss–Hermite moments h_3 and h_4. The left panels show the comparison for the major axis (PA = 53°) with the SAURON measurements for all lenslets whose centres fall inside a 2 arcsec wide 'slit' along the major axis. Individual error bars are not shown. The middle panels show the same comparison, with the SAURON data logarithmically binned in radius, and the errors on the mean included. Central velocity dispersion measurements by Tonry & Davis (1981, asterisk, 3×12 arcsec aperture), Dalle Ore et al. (1991, triangle, 1.5×4.0 arcsec aperture) and Neistein et al. (1999, square, 2 arcsec slit) are shown in the top right corner of the second panel from the top (offset in radius). The right panels show the similar comparison for the minor axis (PA = 143°).
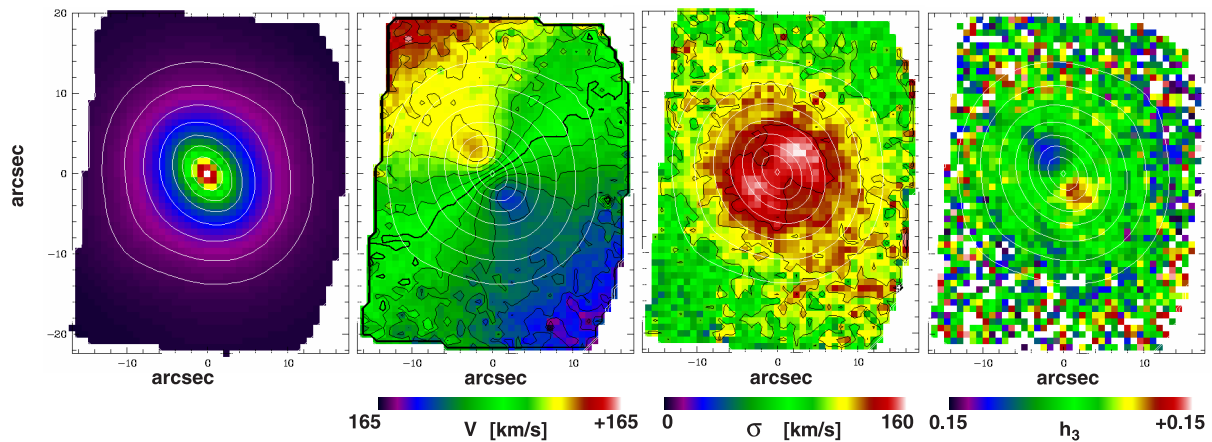
Figure 4. SAURON measurements of the SB0 galaxy NGC 3384, based on a single pointing consisting of four 1800 s exposures. The field-of-view is 33×41 arcsec, and the effective spatial sampling is 0.8×0.8 arcsec. From left to right: (a) reconstructed total intensity I. (b) stellar mean velocity V, with the zero-velocity contour indicated by the thick curve. (c) stellar velocity dispersion σ. (d) Gauss–Hermite moment h_3 which measures the skewness of the line-of-sight velocity distribution. The Gauss–Hermite moment h_4 was measured as well, but varies little over the field, and is not shown. Contours of the reconstructed total intensity are superimposed (in 0.25 mag arcsec^{-2} steps).

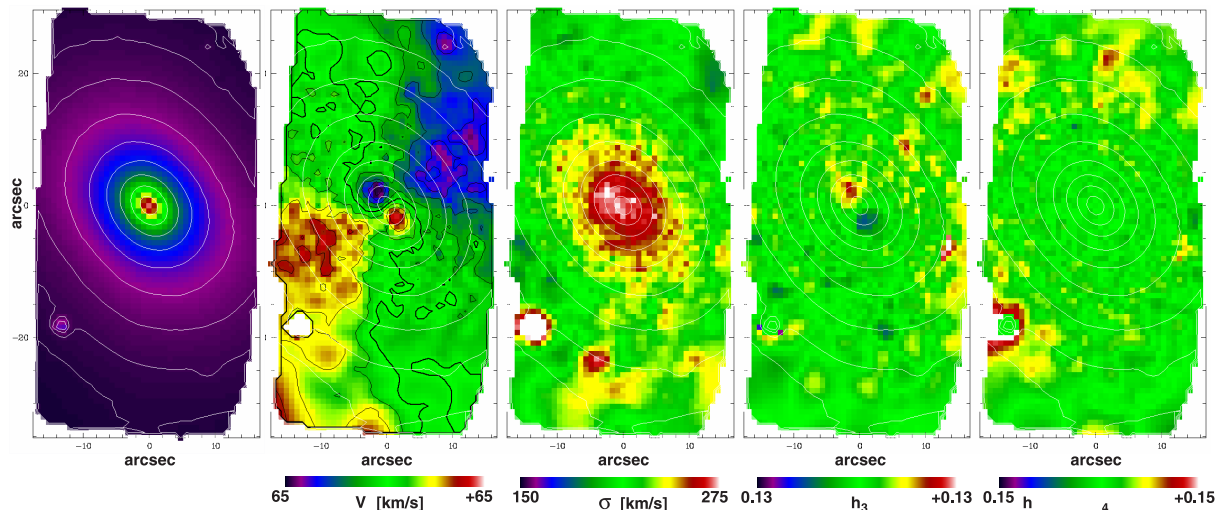**Figure 6.** SAURON observations of the E3 galaxy NGC 4365. From left to right: (a) reconstructed total intensity I; (b) stellar mean velocity V, with the zero-velocity contour indicated by the thick solid curve; (c) velocity dispersion σ; (d) h_3; and (e) h_4. Contours of I are superimposed (0.25 mag arcsec^{-2} per step). The maps are based on two pointings of 4×1800 s each, sampled with 0.8×0.8 arcsec pixels and a ≈ 20 arcsec overlap. The total field of view is 33×63 arcsec. Maps of Mg b and Hβ based on the same observations are shown in Davies et al. (2001).

Fig. 4 displays the resulting integrated intensity, the mean stellar velocity V and velocity dispersion σ, and the Gauss–Hermite moments h_3 and h_4.

Fig. 4(a) illustrates a key advantage of integral-field spectroscopy over traditional aperture and long-slit spectra: by integrating the flux in each spectrum, the two-dimensional surface brightness distribution of the galaxy is recovered. As this is derived from the same data that are used to obtain the kinematics and line strengths, there is no doubt about the relative location of these measurements. A comparison with an *HST*/F555W image taken from the *HST* archive shows excellent agreement, after taking into account the 2.5-arcsec seeing and the spatial sampling of SAURON.

Fig. 4(b) shows that the bulge of NGC 3384 exhibits a regular rotation field. The mean velocities increase steeply along the major axis, reaching ≈ 110 km s^{-1} at $r \approx 4$ arcsec, then decrease slightly, after which they rise again. No velocity gradient is observed along

the minor axis, indicating that the kinematics in the inner region of NGC 3384 is consistent with axisymmetry. The velocity dispersion map (Fig. 4c) shows a symmetric dumb-bell structure with a central depression. Fisher (1997) had already observed the central dip in the minor axis velocity dispersion profile, together with an abrupt change in the h_3 gradient at $r \approx 4$ arcsec along the major axis (cf. Fig 4d). These results strongly suggest the presence of a rapidly rotating inclined inner stellar disc.

Busarello et al. (1996) reported long-slit measurements of V and σ along three position angles. Fisher's (1997) higher signal-to-noise ratio measurements of V, σ, h_3 and h_4 along the major and the minor axes (position angles 53° and 143°) have a spectral resolution very similar to that of SAURON. Fig. 5 compares his results with ours. The column of four panels on the left shows the direct comparison with the SAURON measurements in all the individual lenslets whose centres fall inside the slit used by Fisher. The middle and right-hand columns of panels show the comparison

with the SAURON data now logarithmically binned in radius to increase the signal-to-noise ration. The agreement is good and shows that a 2-hr exposure provides reliable kinematics over the entire SAURON field. Re-sampling our data to the spatial sampling by Fisher results in rms deviations of $7\,\mathrm{km\,s^{-1}}$ in V, $8\,\mathrm{km\,s^{-1}}$ in σ, 0.02 in h_3 and 0.02 in h_4. We do not find systematic offsets for V and h_4. For σ we find mean offsets of $14\,\mathrm{km\,s^{-1}}$ and $7\,\mathrm{km\,s^{-1}}$ (SAURON-Fisher) for the major axis and the minor axis, respectively. Our slightly larger σ values are, however, consistent with the central measurements of Tonry & Davis (1981, asterisk), Dalle Ore et al. (1991, open triangle) and Neistein et al. (1999, open square), as shown in Fig. 5. The h_3 values agree well, except beyond 15 arcsec where the binned SAURON measurements indicate a return to h_3 values with the opposite sign to that of V, as seen in many elliptical galaxies (e.g. Bender et al. 1994). Taking into account the rms variation in Fisher's data, we conclude that the rms errors in the SAURON measurements are $\Delta V \approx 6\,\mathrm{km\,s^{-1}}$, $\Delta\sigma \approx 6\,\mathrm{km\,s^{-1}}$, $\Delta h_3 \approx 0.015$ and $\Delta h_4 \approx 0.015$.

Gebhardt et al. (2000b) reported the presence of a central black hole of $(1.7 \pm 0.8) \times 10^7\,\mathrm{M_\odot}$ in the nucleus of NGC 3384, based on STIS absorption-line spectroscopy. The spatial resolution of the SAURON maps (and of Fisher's long-slit data) is insufficient to resolve the increase in dispersion inside the radius of influence of such a black hole. A dynamical model for NGC 3384 which combines the STIS results with OASIS and SAURON data will provide an accurate determination of the intrinsic shape and internal velocity distribution of the bulge and disc of NGC 3384, and should also increase the accuracy of the black hole mass determination.

3.2 The decoupled core of NGC 4365

NGC 4365 is an E3 galaxy located in the Virgo W cloud just beyond the centre of the Virgo cluster. Surma & Bender (1995) showed that the main body of NGC 4365 rotates around its projected major axis and that its core rotates around the minor axis (cf. Bender 1988; Wagner, Bender & Möllenhoff 1988). The central luminosity profile has a shallow cusp, and the nucleus contains a blue central point source (Carollo et al. 1997).

We observed NGC 4365 with SAURON on the nights of 2000 March 29 and 30. Two pointings of 2 hr each, overlapping by ≈ 20 arcsec on the nucleus, covered a total region of
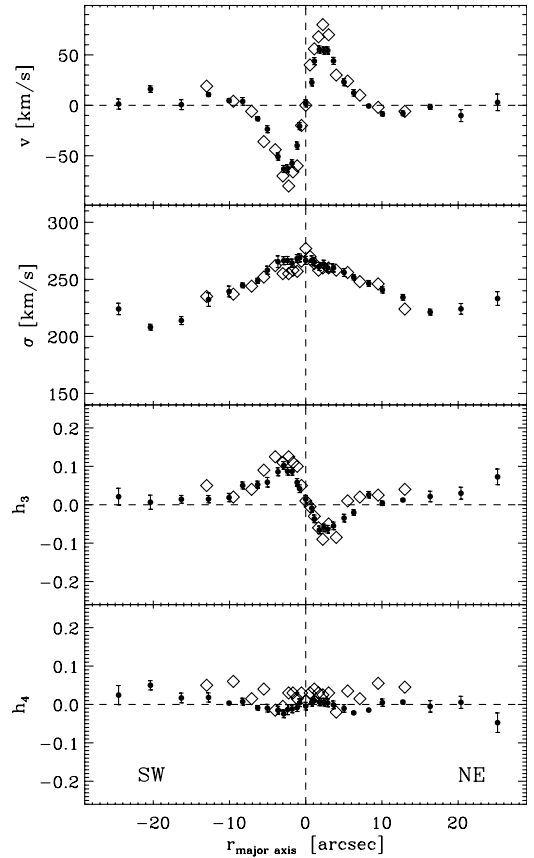

Figure 7. Comparison of the logarithmically binned SAURON kinematics along the major axis of NGC 4365 (dots) with the (binned) long-slit measurements of Surma & Bender (1995, diamonds). From top to bottom: V, σ, h_3 and h_4.

33×63 arcsec. The average seeing during the observations was ≈ 1.6 arcsec (see Davies et al. 2001 for further details). Fig. 6 presents maps of the reconstructed total intensity, the mean stellar velocity V and velocity dispersion σ, and the Gauss–Hermite moments h_3 and h_4.

The mean velocity field displayed in Fig. 6 clearly shows the rich kinematical structure of NGC 4365. As described in Davies et al.
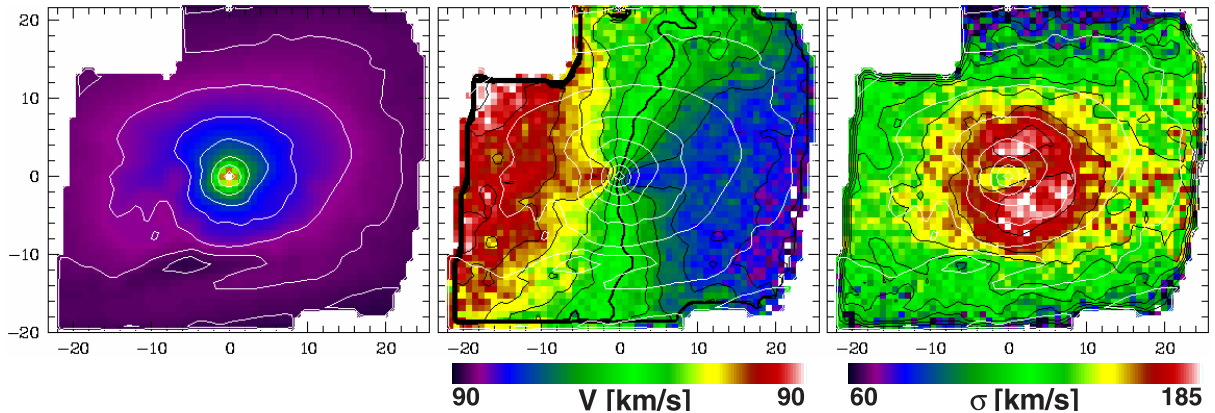

Figure 8. SAURON measurements of NGC 3623 in the Leo triplet, based on two pointings overlapping by ≈ 15 arcsec, and exposed for 4×1800 s each. The field-of-view is 40×50 arcsec and the spatial sampling is 0.8×0.8 arcsec. From left to right: (a) reconstructed total intensity I, (b) stellar mean velocity V, and (c) velocity dispersion σ. Contours of the reconstructed total intensity are superimposed (steps of $0.25\,\mathrm{mag\,arcsec^{-2}}$). They are significantly affected by a dust lane below the nucleus.

(2001), the core measures 7×3 arcsec and rotates around the minor axis, while the bulk of the galaxy rotates approximately around the major axis. The map of the h_3-moment displays a similar two-component structure, with the values anticorrelated with V. The Gauss−Hermite moment h_4 is nearly zero, and shows very little variation over the field. The early long-slit spectroscopy had revealed the global kinematic structure of NGC 4365, but the SAURON maps make it possible to determine, for example, the position angle of the rotation axis accurately. It is aligned with the minor axis in the core, but misaligned from the major axis by $12° \pm 2°$ in the outer regions. This is a strong indication of a triaxial intrinsic shape (cf. Statler 1991), possibly containing a nearly axisymmetric core. Construction of a triaxial dynamical model for this object is in preparation.

The individual SAURON measurements along the major axis can be compared with the long-slit data from Surma & Bender (1995), obtained with a 1.4-arcsec slit and binned radially to obtain a sufficient signal-to-noise ratio. The original data could not be retrieved, so we scanned the published figure. Fig. 7 shows that the agreement is excellent. The mean velocity curves agree very well outside 3 arcsec. Inside this radius there are differences in the peak amplitude and the slope of the central gradient, but they are consistent with the different values of the seeing. Resampling our data to the spatial sampling used by Surma & Bender (1995) results in rms deviations of $13\,\mathrm{km\,s^{-1}}$ in V, $6\,\mathrm{km\,s^{-1}}$ in σ, and 0.02 in h_3 and h_4. We ascribe the rather large rms deviation for V to the different seeing. We do not find significant systematic offsets for V, σ and h_3. For h_4 we find a systematic offset of 0.03 in the sense that our measurements are smaller. This may be due to differences between the template stars used in the two studies.

3.3 A central stellar disc in NGC 3623

NGC 3623 (M 65) is a bright, large, highly inclined SAB(rs)a galaxy located in the nearby Leo I group ($M_B = -20.8$, $D_{25} = 9.8$ arcmin, $i \approx 75°$). It forms the Leo triplet together with NGC 3627 and 3628, and it is classified as a LINER (e.g. Ho, Filippenko & Sargent 1997). While there are strong indications that NGC 3627 and 3628 are interacting, NGC 3623 appears undisturbed (e.g. Chromey et al. 1998 and references therein). It is one of the galaxies discussed by Hubble (1943) in his paper on the sense of rotation of spiral arms, and is included in the Hubble Atlas (Sandage 1961).

Surprisingly, despite its closeness, the kinematics of NGC 3623 has received little attention. The only available absorption and emission-line kinematics dates back to Burbidge, Burbidge & Prendergast (1961). All H I kinematic data are at low spatial resolution (e.g. Krumm & Salpeter 1979) or deal with the H I distribution of the entire group (e.g. Rots 1978). Most spectroscopic observations of NGC 3623 are concerned with emission-line ratios, to probe the ionization mechanism of the gas and the nuclear activity (from Burbidge & Burbidge 1962 to Bresolin, Kennicutt & Garnett 1999). The observations reported here offer the first view of the stellar kinematics of the bulge of NGC 3623.

We observed NGC 3623 on 2000 March 30 and 31, and obtained a mosaic of two fields with substantial overlap on the nucleus. Each field was exposed for $4 \times 1800\,\mathrm{s}$ and the resulting mosaic covers most of the bulge. The seeing was ≈ 1 arcsec. The SAURON total intensity, velocity, and velocity dispersion maps are shown in Fig. 8 (cf. Bureau et al. 2001). The main dust lane is easily visible in the SAURON reconstructed image. It appears as the dark band covering the bottom 25 per cent of the field (the position angle of

the major axis of the galaxy is roughly horizontal in Fig. 8). The velocity field shows a typical rotation pattern, but also reveals twists in the kinematic minor axis and a gradient along the minor axis ('minor-axis rotation'). This is not unexpected, as NGC 3623 is barred. There may be a contribution from a warped stellar disc. However, it is difficult to estimate how much of this structure is affected by the dust extinction. One feature which is certainly not due to dust is the central stellar disc, clearly visible as a flattening of the isovelocity contours in the centre of the galaxy. This disc is also easily seen in the velocity dispersion map. While the dispersion increases steadily towards the centre, roughly following the isophotes, there is a pronounced elongated depression in the centre. This is the expected signature of a flattened, cold component embedded in the bulge. The small thickness observed suggests that the central disc is thin and located in the equatorial plane of the galaxy (nearly edge-on). Both the central stellar disc and the large scale disc are likely coplanar. The h_3 map (not shown) shows a sign reversal at about $6-8$ arcsec on the major axis, confirming the size of the central disc apparent from Fig 8(b−c).

Many of the galaxies observed so far with SAURON show similar evidence for a central stellar disc. However, most appear thicker than in the case of NGC 3623. This is most likely a result of projection effects, the discs being more nearly face-on, but could also be due to the presence of intrinsically thick discs. The maps of NGC 3623 provide a further illustration of the advantages of integral-field spectroscopy. By contrast to spectroscopy along a few slits, the SAURON maps allow us to delineate the entire (projected) kinematics of any embedded subsystem.

3.4 HR mode observations of M32

M32 is a high-surface brightness, compact E3 companion of the Andromeda galaxy. In the past two decades, M32 has been scrutinized extensively for the presence of a central black hole, with ever-higher spatial resolution and increasingly sophisticated dynamical modelling (Dressler 1984; Tonry 1984, 1987; Dressler & Richstone 1988; van der Marel et al. 1994; Qian et al. 1995; Bender, Kormendy & Dehnen 1996; van der Marel et al. 1997a,b, 1998; Joseph et al. 2001).

We observed M32 on 1999 October 15, with the principal aim of testing the HR mode of SAURON. The seeing was ≈ 0.95 arcsec. Fig. 9 shows the integrated intensity, stellar mean velocity, velocity dispersion and Gauss−Hermite moment h_3 of the central 9×11 arcsec, derived from a single 2700-s exposure. The velocity field is very regular, has a peak amplitude of about $50\,\mathrm{km\,s^{-1}}$, and is consistent with axisymmetry. The h_3-field is similarly very regular, and h_3 has the opposite sign of V everywhere. The velocity dispersion in M32 is smaller than the HR-mode instrumental dispersion of $\approx 105\,\mathrm{km\,s^{-1}}$ (Paper I), except in the inner arcsecond (e.g. van der Marel et al. 1994, 1997a; Joseph et al. 2001). For this reason it is difficult to measure h_4. It varies little over the field, and we do not show it here.

The plus sign in the M32 maps indicates the position of strong [O III] emission, with a velocity close to the systemic velocity of M32. It is not spatially resolved and most likely originates in a planetary nebula in M32.

Fig. 10 compares the SAURON measurements with the long-slit observations of van der Marel et al. (1994), using ISIS at the same Cassegrain port, with similar seeing, but with an instrumental dispersion of $8\,\mathrm{km\,s^{-1}}$. The SAURON HR measurements were axisymmetrized and binned in the same way as the ISIS data. The agreement is excellent: the differences SAURON-ISIS are $2.3 \pm$
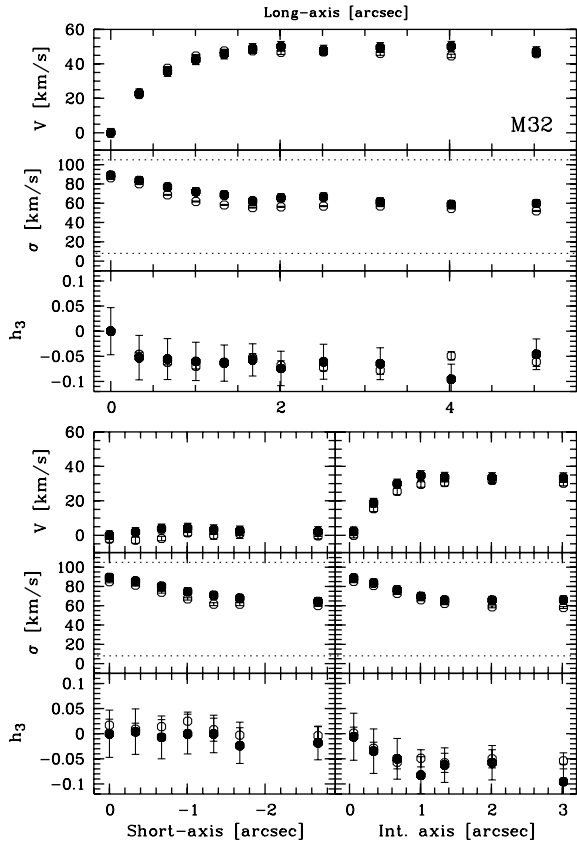
Figure 10. Comparison of the SAURON kinematics of M32 (solid dots) with the ISIS long-slit measurements of van der Marel et al. (1994), taken with similar seeing but with superior spectral resolution (open circles). Top: major axis, PA = 160°. Bottom left: minor axis, PA = 71°. Bottom right: intermediate axis, PA = 116°. The data have been folded about the centre. The horizontal dotted lines in the σ-panels indicate the instrumental resolutions.

$2.2 \, \mathrm{km \, s^{-1}}$ in V, $6.0 \pm 2.6 \, \mathrm{km \, s^{-1}}$ in σ, and -0.009 ± 0.016 in h_3. The observed σ is well below the SAURON instrumental dispersion, but can still be determined reliably over the entire HR field of view, albeit with a small systematic offset.

Van der Marel et al. (1998) constructed fully anisotropic axisymmetric models for M32 by means of Schwarzschild's (1979) orbit superposition technique. The models fit the surface brightness distribution, high signal-to-noise ratio ground-based long-slit kinematics along multiple position angles, and Faint Object Spectrograph (FOS) measurements. They require a central black hole of mass $(3.4 \pm 0.7) \times 10^6 \, \mathrm{M_\odot}$ but do not constrain the inclination of M32 strongly: models with $i = 55°$ and $i = 90°$ fit the measurements equally well.

Our HR mode data shows that the stellar velocity field of M32 is accurately symmetric with respect to the minor axis of the surface brightness distribution, as expected in axisymmetric geometry for any inclination angle. The position angle of the zero velocity curve is within 2° of the minor axis of M32. This suggests that there is no compelling reason to consider triaxial models for M32, and that the black hole mass determination is robust.

4   GAS KINEMATICS

The wavelength range 4810–5350 Å of the SAURON spectra allows observation of the Hβ, [N I] and [O III] emission lines in nearby

objects. Paper I showed an example of the non-axisymmetric distribution of [O III] in NGC 3377. Here, we consider NGC 5813 and compare the properties of the emission-line gas as derived from our SAURON observations with long-slit data from the literature. We also discuss NGC 7742, in which we have detected a gaseous ring which counter-rotates with respect to the central stellar component. We first describe the algorithm we use to measure the emission lines. This expands on the brief outline presented in section 5.3 of Paper I.

4.1   Measurement of the emission lines

The emission lines need to be disentangled from the stellar absorption line spectrum of a galaxy. We use an algorithm similar to the one employed by Emsellem & Goudfrooij (in preparation, see also Goudfrooij & Emsellem 1996), which consists of the following iterative steps:

(i) We first derive the stellar kinematics (V and σ) using the FCQ algorithm and a single stellar template spectrum (typically that of a K0 giant), and truncate the spectral domain when the brightest emission lines (e.g. [O III], Hβ) influence the results. The resulting maps are then median filtered to remove residual spurious values due to, for example, a low signal-to-noise ratio or, more likely, the presence of a strong emission line.

(ii) We then build a spectral library, including both stellar and galactic spectra (devoid of detectable emission lines) in the same spectral domain but at higher spectral resolution than that of the SAURON data cube. A linear combination of these spectra is fitted to each spectrum in the SAURON data cube while masking out regions where emission lines may contribute, and taking into account the measured differences in V and σ.

(iii) We then subtract the fitted spectra to obtain – in principle – a pure emission-line data cube. All lines are simultaneously fitted using Gaussians of the same velocity and width, by means of dedicated software.

(iv) Finally, we subtract the fitted emission-line data cube from the original SAURON data cube to obtain pure stellar absorption-line spectra.

This procedure generally works well with only two iterations. It is very effective in recovering faint emission and is superior to narrow-band imaging. Problems may occur when, for example, the emission lines have non-Gaussian profiles, or when they do not probe the same physical regions. These problems can be solved during step (iii) by generalizing the fitting functions and/or relaxing the fitting constraints. A more serious problem may come from the lack of proper stellar types in the spectral library (e.g. super metal-rich stars). This can result in over- or underestimated emission-line fluxes, particularly in the case of the faint [N I] $\lambda 5200$ doublet which usually lies close to the strong Mg b absorption lines. As a result, the library has to be tuned to each galaxy and sometimes even to different regions within a galaxy.

4.2   The emission-line gas in NGC 5813

NGC 5813 is a large and bright elliptical galaxy classified as E1-2 in the RC3 ($M_B = -20.99$, $T = -4.5$ in LEDA). It is located in the Virgo–Libra Cloud (Tully 1988), near NGC 5814 and NGC 5806. The surface brightness profile of NGC 5813 has a core with nuclear cusp slope $\gamma^V_{\mathrm{phys}} = 0.24 \pm 0.03$ (Carollo et al. 1997). The ellipticity increases with radius, and the galaxy displays isophotal twists (Lauer et al. 1995; Carollo et al. 1997). NGC 5813 contains a
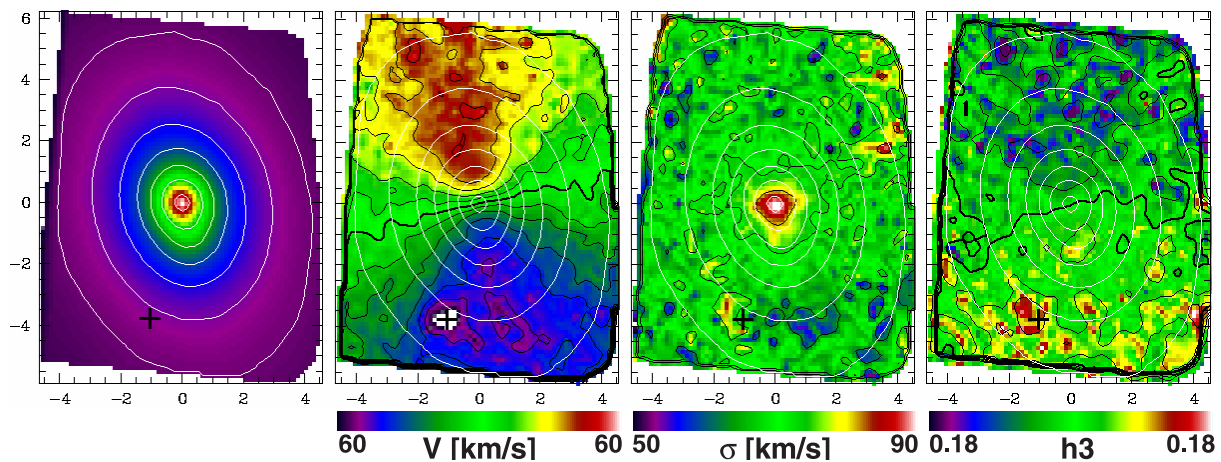
Figure 9. SAURON measurements of M32, based on a single 2700 s exposure with the HR mode. The field of view is 9×11 arcsec, and the spatial sampling is 0.27×0.27 arcsec. From left to right: (a) reconstructed total intensity, with isophotal contours shown in steps of 0.25 mag arcsec^{-2}. (b) Stellar mean velocity V, with the zero-velocity contour indicated by the solid curve. (c) stellar velocity dispersion σ. (d) Gauss–Hermite moment h_3. The + indicates the location of the planetary nebula discussed in the text.
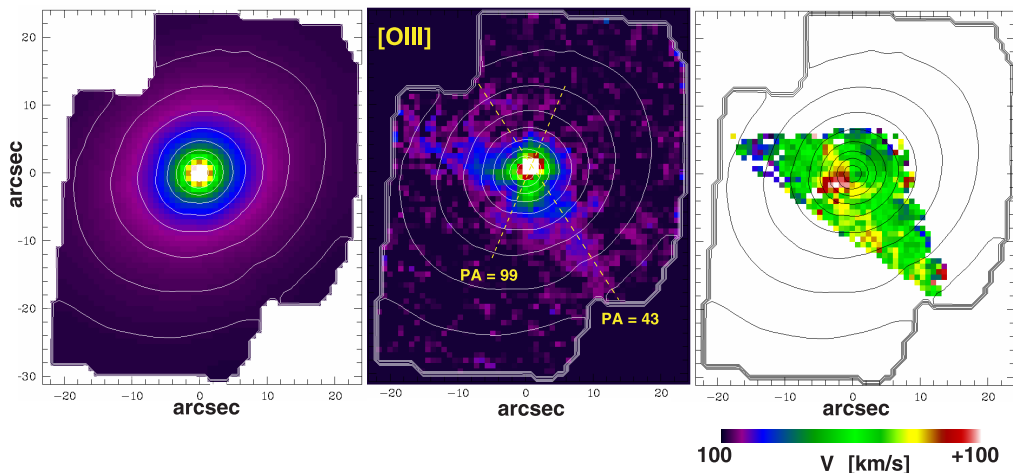

Figure 11. SAURON measurements of the [O III] emission in NGC 5813. From left to right: (a) reconstructed total intensity of the stellar continuum light; (b) intensity of [O III] emission; and (c) velocity field of the emission-line gas. The maps are based on two pointings of 4×1800 s each, sampled with 0.8×0.8 arcsec pixels. The dashed lines in the middle panel indicate the position angles of the Hα + [N II] long-slit spectroscopy by Caon et al. (2000), shown in Fig. 12.

rapidly rotating central component within the inner $\lesssim 7$ arcsec, has negligible rotation at larger radii, and shows weak evidence for minor-axis rotation (Efstathiou, Ellis & Carter 1980, 1982). The galaxy is undetected in H I or CO, but has an unresolved, weak central radio continuum source (6 cm; Birkinshaw & Davies 1985; Wrobel & Heeschen 1991). It was also detected by *IRAS* in the 12- and 100-µm bands (Thronson, Bally & Hacking 1989), although many authors report non-detections (e.g. Knapp et al. 1989). Emission-line ratios are typical of LINERS but no X-ray emission is detected (Ho, Filippenko & Sargent 1997).

HST imaging of NGC 5813 has revealed a dust lane parallel to the major axis, east of the nucleus, and dust filaments inside 7 arcsec, i.e., inside the decoupled core (e.g. Carollo et al. 1997). The distribution of emission-line gas, as traced by Hα + [N II] narrow-band imaging, is very elongated and bent: it extends along the minor axis at position angle (PA) = 43° on one side, but follows PA = 190° on the other side (Caon, Macchetto & Pastoriza

2000). This is similar to the shape of the region where the $B - R$ colour is affected by dust (Peletier 1989).

We observed NGC 5813 on 2000 March 29 and 30 and April 4, obtaining a mosaic of two fields exposed for 4×1800 s each, with overlap on the nucleus. The seeing was 1 arcsec on the first two nights and 2.5 arcsec on the last. Fig. 11(a) shows the reconstructed stellar continuum intensity derived from our SAURON mosaic. Fig. 11(b) shows the integrated intensity map of [O III]. Its morphology resembles that of the Hα + [N II] map of Caon et al. (2000) and exhibits a complex filamentary structure, most likely not (yet) in equilibrium with the potential of the central region. This is confirmed by the SAURON velocity map (Fig. 11c), which does not display a simple pattern.

The SAURON gas kinematics can be compared with the kinematics of Hα + [N II] obtained by Caon et al. (2000) along two position angles. In order to be consistent with the SAURON kinematics (for both the stars and the gas), we had to offset the
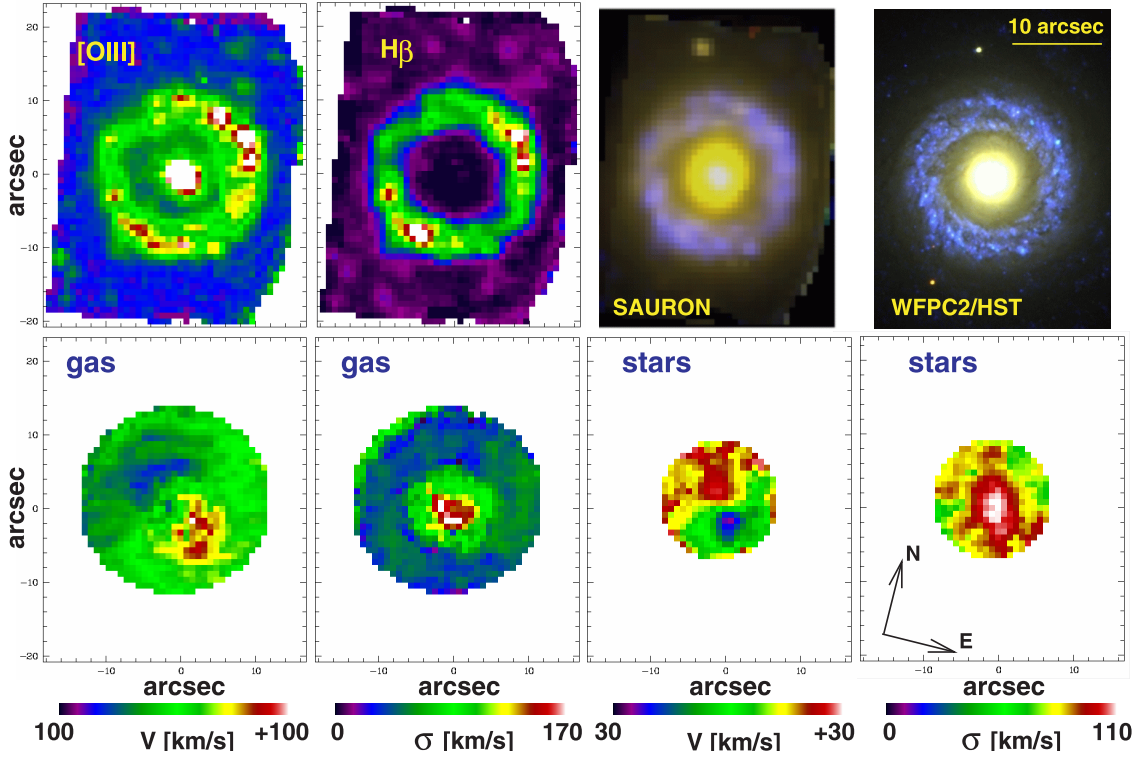
Figure 13. SAURON maps of NGC 7742, based on 1 pointing, exposed for $3 \times 1800 + 1 \times 900$ s. The field-of-view is 33×41 arcsec and the spatial sampling is 0.8×0.8 arcsec. The top panels show the emission-line intensity distributions of [O III] and Hβ, followed by a colour-coded reconstructed image composed of [O III] (blue), blue continuum (green), red continuum (red) derived from the SAURON data, and a similar colour-coded image composed of *HST*/WFPC2 exposures with the F336W (blue), F555W (green) and F814 (red) filters. The bottom row shows (from left to right) the derived gas velocity and velocity dispersion fields, and the stellar velocity and velocity dispersion fields.
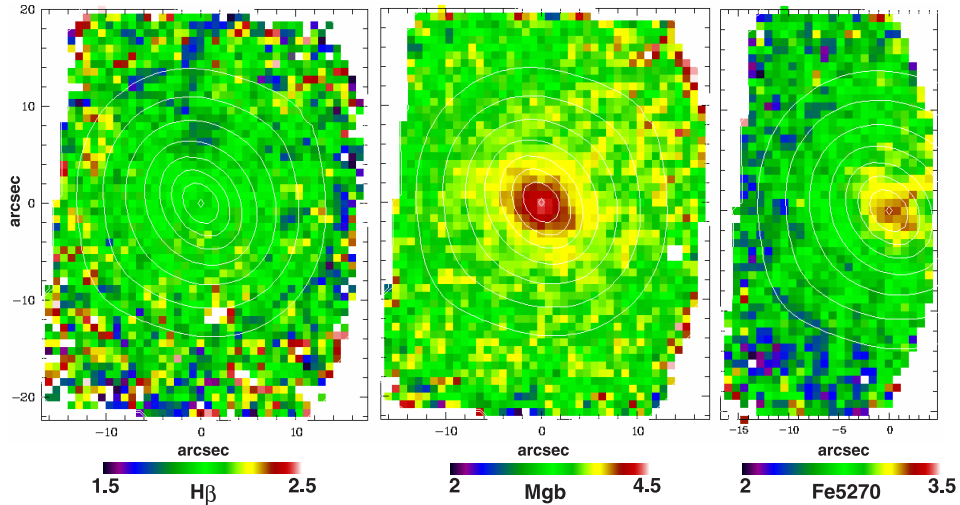

Figure 14. SAURON line-strength maps of NGC 3384, derived from the exposures described in Fig. 4. From left to right: (a) Hβ, (b) Mg b and (c) Fe5270. Contours of constant reconstructed intensity of the stellar continuum light are superimposed.

Caon et al. data by $+70 \, \mathrm{km \, s^{-1}}$. Fig. 12 shows that the rms deviations increase from $\approx 17 \, \mathrm{km \, s^{-1}}$ in the centre to $\approx 50 \, \mathrm{km \, s^{-1}}$ at the outermost measured points.

4.3 The extended emission-line gas in NGC 7742

NGC 7742 is a face-on spiral classified as S(r)b in the RC3 ($M_B = -19.76, T = 1.3$ in LEDA). It probably forms a binary system

with NGC 7743 in the Pegasus Cloud (Tully 1988; Honma 1999) and is a good example of the latest spirals included in our sample. De Vaucouleurs & Buta (1980) first identified the inner stellar ring and Pogge & Eskridge (1993) detected a corresponding small, bright ring of H II regions with faint flocculent spiral arms (see also Wozniak et al. 1995). NGC 7742 also possesses a significant amount of neutral hydrogen, molecular gas, and dust (e.g. Roberts et al. 1991). It shows essentially no sign of departure from axisymmetry (Rix & Zaritsky
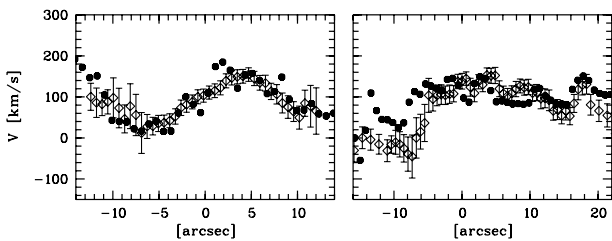
Figure 12. Comparison of the SAURON [O III] velocities (filled squares) with those derived by Caon et al. (2000), based on Hα + [N II] measurements at PA = 43° and PA = 99° (open squares). We have offset the Caon et al. velocity measurements by 70 km s^{-1} to be consistent with the SAURON kinematics.

1995; Kornreich, Haynes & Lovelace 1998). It is classified as a transition LINER/H II nucleus object (Ho, Filippenko & Sargent 1997).

We observed NGC 7742 with SAURON on the night of 1999 October 13. We obtained $3 \times 1800 + 1 \times 900$ s on one field centred on the galaxy. The seeing was 1.5–2.5 arcsec. The spectra reveal emission from Hβ, [O III], and [N I]. The detection of the [N I] doublet is rather difficult because we expect the line to be about 10 times less luminous than Hβ, and it lies close to the red edge of the Mgb triplet. Fig. 13 shows the intensity in [O III] and Hβ, together with the derived velocity and velocity dispersion fields. Most of the emission is confined to a ring which coincides with the flocculent spiral arms. The Hβ line is clearly dominant in the ring, with [O III]/Hβ ranging from 0.06 to 0.14. We also detect all three sets of lines at the centre, but this time with [O III]/Hβ ≈ 1.0 ± 0.1.

Also shown is a colour-coded reconstructed image composed of [O III] (blue), blue continuum (green), red continuum (red) derived from the SAURON data cube, and a similar colour-coded image composed of *HST*/WFPC2 exposures with the F336W (blue), F555W (green) and F814W (red) filters (GO 6276, PI J. Westphal). The SAURON map does not have the spatial resolution of *HST*, but it does demonstrate that our analysis technique is capable of providing accurate emission-line maps.

The main surprise comes from the comparison of the stellar and gas kinematics: the gas in the ring counter-rotates with respect to the stellar component inside the radius of the ring. The amplitude of the stellar velocities is modest, because the galaxy is seen close to face-on, but the zero velocity curve is well-defined, and oriented at PA = 42° ± 12°. This is consistent with the zero velocity curve of the gas, which is at PA = 35° ± 5°. The stellar velocities outside and in the ring itself are consistent with being equal to the systemic velocity, although any velocity difference of the order of 30 km s^{-1} is difficult to detect in these regions because of the lower signal-to-noise ratio of the spectra and/or the emission line contamination. The signs of stellar and gas velocities inside the ring are, however, clearly opposite. The ring-like structure in the gas appears as a tightly wound multi-arm spiral structure, reminiscent of nuclear (< 1 kpc) resonant rings (Buta & Combes 1996). High-resolution infrared images would be invaluable to attempt the detection of a non-axisymmetric (weak bar) component in the older stellar population. The spirals can be followed in the *HST* images into the central arcsecond via the dust absorption features. If we assume they correspond to a trailing wave, then the near side is in the north-east quadrant.

5   LINE-STRENGTH MAPS

The SAURON wavelength coverage allows measurement of the line-strength indices Hβ, Mg b, and Fe5270 in the Lick/IDS system

(Worthey et al. 1994; see also Paper I). These indices, in combination with simple stellar population models, can be used to estimate luminosity-weighted metallicities and ages. Two-dimensional line-strength maps make it possible to study the shape of the contours of constant line-strength, and consequently of constant metallicity and age (see, e.g. Peletier et al. 1999; del Burgo et al. 2001). Davies et al. (2001) presented and discussed such maps for NGC 4365. Here, we consider the observed line-strength distributions in NGC 3384 and 5813, based on the observations described in Sections 3.1 and 4.2, and compare them with previous long-slit measurements.

5.1   Measurement of absorption line strengths

Line strengths, as measured in the Lick/IDS system, are a measure of the flux in a central bandpass compared to a continuum defined by two sidebands. Two steps are required to convert measured equivalent widths to line-strength indices on the Lick/IDS system: (i) a correction for the difference in spectral resolution, and (ii) a correction for the stellar velocity dispersion of the galaxies. We correct for the difference in resolution by smoothing the data to the resolution of the Lick/IDS system, 8.4 Å in the SAURON wavelength range (Worthey & Ottaviani 1997). Absorption-line indices for stars measured in this way should be on the Lick/IDS system, apart from small offsets (≲ 0.15 Å) that arise because the Lick/IDS system is not based on flux-calibrated spectra (e.g. Vazdekis et al. 1997). In future papers we will use our full sample of galaxy observations to establish the significance of any offsets in the line-strength indices compared to the Lick/IDS system.

In order to correct the line strengths for the broadening caused by the stellar velocity distribution, we convolved a template star spectrum with the observed line-of-sight velocity distribution of the galaxy at each position (see Section 3), and derived the correction necessary to evaluate the indices at zero velocity dispersion. This correction does not depend critically on the stellar type or temperature for G and K stars (e.g. Davies et al. 1993).

5.2   The effect of sky subtraction errors

Accurate sky subtraction is achieved using the 146 lenslets located 1.9 arcmin away from the main field that record sky spectra simultaneously with the object spectra (Paper I). Some of the galaxies are so large that even at this separation the galaxy contribution is non-negligible. The error caused by this 'galaxy-contaminated' sky is however smaller than the typical Poisson errors. For example, for NGC 3384 the galaxy contribution in the sky field is roughly a factor of 40 smaller than in the corner of the SAURON field (25 arcsec). When one subtracts the spectrum in the sky field from a spectrum at 25 arcsec, one also subtracts the galaxy contribution. In the worst case this would introduce a relative line-strength error of 2.5 per cent. Since, however, line-strength gradients are fairly gentle, this is a generous overestimate of the error. For the larger galaxy NGC 5813, the difference in galaxy surface brightness between the edge of the SAURON field and the sky is only a factor of 10, which means that the maximum relative error in the indices at the edge of the frame is at most 10 per cent. In practice it will be smaller than 5 per cent.

5.3   NGC 3384

Fig. 14 shows the maps of Hβ, Mg b and Fe5270 for NGC 3384, obtained with the procedure described in the above. As a result of

the effect of a slightly tilted interference filter, the observed wavelength range varies over the field of view (Paper I, section 4.9). This variation affects only the extent of the spectra, and impacts our measurements of the Fe5270 index for galaxies with significant recession velocities. For most galaxies in our sample, the wavelength range of the red sideband is included in the SAURON data for about 2/3 of the field of view. We illustrate this effect in Fig. 14(c). We have taken a conservative approach showing only measurements which are completely unaffected by the decrease in wavelength-coverage. In future work we intend to improve the data-reduction procedure, and increase the effective field of view for this index.

Fisher, Franx & Illingworth (1996) published accurate line-strength indices for NGC 3384, tabulating amongst other indices Hβ, Mg b and Fe5270 on the Lick/IDS system. Their spectra had 3.1-Å (FWHM) spectral resolution ($\sigma_{inst} \simeq 75\,km\,s^{-1}$), and were taken with a 2-arcsec slit along the major and minor axes (PA = 53° and 143°). Measurements of the Fe5270 index are only available for the major axis. Fig. 15 shows the comparison with simulated long-slit measurements derived from the SAURON data-cubes. The SAURON data are binned logarithmically in radius to
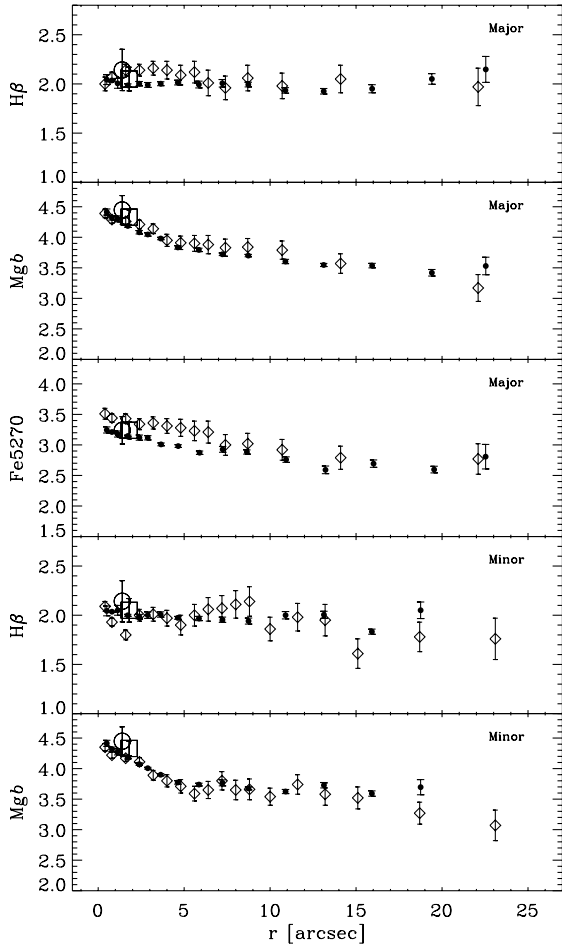
produce a similar number of data points. Fisher et al. (1996) folded their measurements about the centre and we have followed the same procedure to make this comparison.

The agreement for both Mg b and Hβ is excellent. Re-sampling our data to the spatial sampling of the Fisher et al. (1996) data results in rms deviations of 0.1 Å in Mg b and 0.1 Å in Hβ. The systematic offsets are less than 0.03 Å. The comparison for the Fe5270 index shows a systematic offset of ~ 0.24 Å in the sense that our data show weaker Fe5270, which is however more in line with the expected value for a galaxy of this luminosity (Davies et al. 1993). The rms deviations are 0.1 Å. The offset is modest and the overall gradient is consistent with the data of Fisher et al. (1996). There is good agreement with the central measurements by Trager et al. (1998, large open circle) and Kuntschner et al. (2001, large open square). The agreement between the Fe5270 index in NGC 5813 (see below) and published data reinforce our confidence in these measurements.

The SAURON maps show that Mg b is enhanced in the region defined by the inner major-axis disc ($r \lesssim 5$ arcsec). Outside this region there is a weaker gradient. This supports the interpretation that later infalling components (i.e. the material that formed the disc) are made out of enriched material (as in NGC 4365, Davies et al. 2001). The same is seen in Fisher et al.'s data. In the region between 4 and 10 arcsec, the contours of equal Mg b line strengths have the same shape as the isophotes of the stellar surface brightness distribution. Hβ is roughly constant everywhere (as in NGC 4365). However, NGC 3384 shows an unusually strong Hβ index, ~ 2.0 Å, which indicates a luminosity-weighted age of ~ 5 Gyr younger than that of the oldest elliptical galaxies. Unlike the disc, the other prominent central component, the inner bar (e.g. Busarello et al. 1996) is not seen in the line-strength maps. Martin & Roy (1994) proposed that bars smear out population gradients, based on a correlation between bar strength and radial O/H abundance gradient in the young stellar population derived from individual H II regions. To date, it has not been possible to verify this correlation using gradients in the absorption line strengths, which sample the entire stellar population. Statistical analysis for the entire SAURON sample will have to show whether radial abundance gradients are affected by the presence of bars.

5.4 NGC 5813

Early measurements of the line-strength profile in NGC 5813 are reported in Efstathiou & Gorgas (1985), and modelled in Aragón, Gorgas & Rego (1987). Superior measurements were published by Gorgas, Efstathiou & Aragon–Salamanca (1990), based on a 34 200-s major axis exposure on the Anglo-Australian Telescope (AAT) with the Image Photon Counting System (IPCS) and a 3-arcsec slit (cf. Efstathiou et al. 1980, 1982). They present, among other indices, the Hβ, Mg b and Fe5270 index. González (1993) also reports these indices, for the major and minor axes (2.1-arcsec slit).

Fig. 16 shows the comparison of the SAURON measurements with those by Gorgas et al. (1990) and González (1993). The overall agreement is good. The comparison for Hβ is excellent, even in the central regions where nebular emission severely affects the Hβ index. This can be seen at $r \approx 2.5$ arcsec where all data sets show a dip in Hβ absorption strength. Re-sampling our data to the spatial sampling of the published data results in rms deviations of ~ 0.25 Å and systematic offsets $\lesssim 0.1$ Å for the González data. The comparison with Gorgas et al. shows rms deviations of up to 0.45 Å and systematic offsets of up to 0.6 Å. However, this is consistent

Figure 15. Comparison of the SAURON Hβ, Mg b and Fe5270 line-strengths for NGC 3384 (dots) with the measurements by Fisher, Franx & Illingworth (1996, open diamonds) along the major (PA = 53°) and the minor (PA = 143°) axis. The large open circle at $r = 1.4$ arcsec indicates the Lick observation (Trager et al. 1998) and the large open square at $r = 1.8$ arcsec represents the data of Kuntschner et al. (2001). The SAURON data are binned logarithmically in radius along a simulated slit of 2-arcsec width.
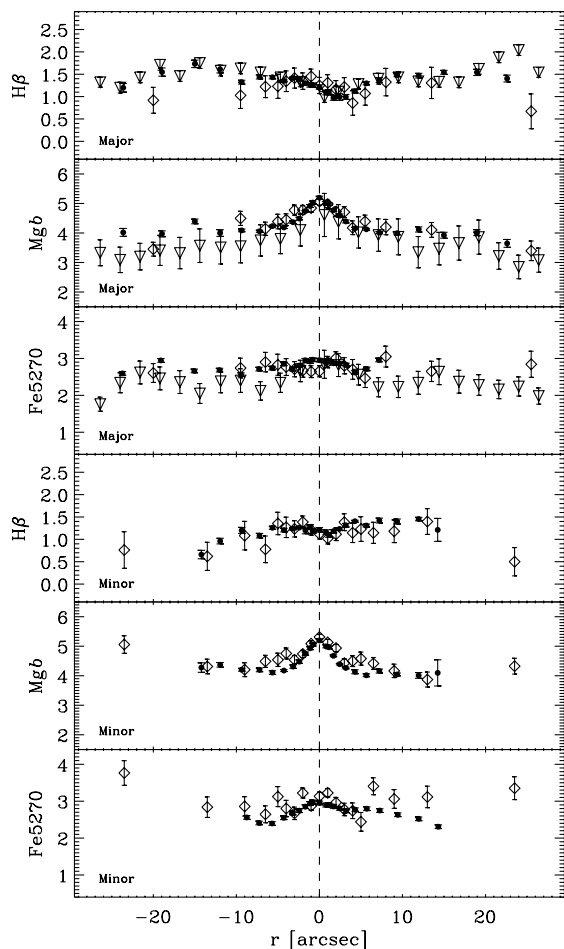
Figure 16. Comparison of the SAURON Hβ, Mg b and Fe5270 line-strengths for NGC 5813 (3-arcsec simulated slit, filled circles) with the measurements by Gorgas et al. (1990, Run 2, open triangles) and González (1993, open diamonds), for the major and minor axis.

with the error bars given by Gorgas et al. Overall, the comparison for NGC 5813 shows larger rms deviations than the comparison for NGC 3384. We ascribe this to the effects of nebular emission and slightly larger errors in the literature data.

Fig. 17 displays the SAURON maps of mean stellar velocity, Mg b, and Hβ observed and corrected for emission for NGC 5813, in all cases with contours of the stellar continuum intensity superimposed. The rapidly rotating core is clearly visible, and extends ≈ 12 arcsec along the major axis and ≈ 7 arcsec along the minor axis. The zero-velocity curve is nearly straight, and is misaligned by $13 \pm 2°$ from the minor axis of the surface brightness distribution. The Mg b distribution has a peak in the region of the rotating central disc, and a very shallow gradient outside it, similar to NGC 3384 and 4365. Hβ here is severely affected by emission lines (see Section 4), so needs to be corrected for the emission before studying the stellar populations. The two-dimensional structure of the emission can clearly be seen in Fig. 17(c). We have subtracted the emission contamination from the spectra by means of an optimal template fitting routine. The 'emission-free' Hβ map is shown in Fig. 17(d). This shows that the stellar absorption of Hβ is roughly constant over the whole field, similar to what we found for NGC 4365 (Davies et al. 2001).

6   CONCLUSIONS

We built SAURON to measure the intrinsic shapes and internal velocity and metallicity distributions of early-type galaxies. This is a key component of a comprehensive study of the internal structure of these systems, aimed at gaining insight into the connection between the kinematics and stellar populations, and the relation between nuclear and global properties. Accordingly, we are carrying out a representative survey of nearby early-type galaxies covering a large range of luminosity and ellipticity, and so covering a range of environment, nuclear cusp slope and rotational support.

The full survey will not be completed until later on in 2002, but the first results presented here demonstrate that the SAURON measurements agree with previous high-quality long-slit kinematic and line-strength measurements. This establishes the scientific integrity of the instrument. It also shows that integral-field spectroscopy is a mature technique, superior to long-slit studies because of the fundamental advantage of complete spatial coverage.

A preliminary analysis of the survey maps shows that early-type galaxies display a variety of line-strength distributions and kinematic structure which appears richer than often assumed. We have shown specific examples of minor axis rotation, decoupled cores, central stellar discs, and non-axisymmetric and counter-rotating gaseous discs. The provisional indication is that only a
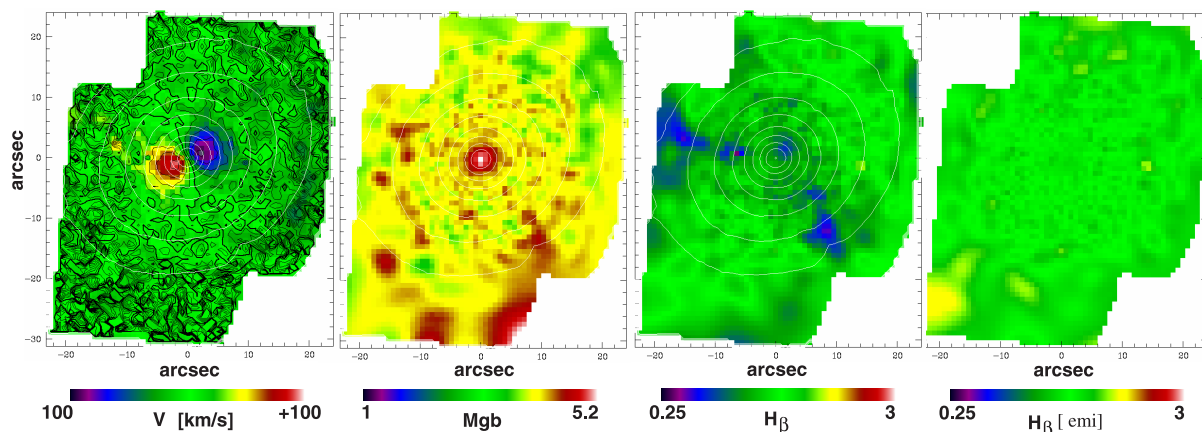

Figure 17. SAURON maps of NGC 5813, derived from the two pointings described in Fig. 12. From left to right: (a) stellar absorption-line velocity field, (b) Mg b, (c) Hβ observed and (d) Hβ corrected for emission. The contours of constant integrated intensity of the continuum light are superimposed.

small fraction of these galaxies can have axisymmetric intrinsic shapes. The line-strength distributions appear to follow the surface brightness distribution closely.

We have started to complement the SAURON maps with high-spatial-resolution spectroscopy of the nuclear regions, using OASIS. STIS spectroscopy for many of the sample galaxies is available in the *HST* archive. Radial velocities of planetary nebulae and/or globular clusters in the outer regions have been obtained for some of the galaxies in our sample, and many more will become available to about $5R_e$ with a special-purpose instrument now under construction (Freeman et al., in preparation).

We are analysing the SAURON maps by Fourier techniques. This will provide the ellipticity, position-angle, and deviations from the elliptic shape of the contours of constant velocity dispersion, h_4 and line strengths, as a function of radius (Copin et al. in preparation). This approach has been customary for the analysis of the surface brightness distribution of early-type galaxies (e.g. Kormendy & Djorgovski 1989). The maps of mean velocity and h_3 can be quantified in a similar way, just as is possible for H I and CO data (Franx, van Gorkom & de Zeeuw 1994; Schoenmakers, Franx & de Zeeuw 1997; Wong 2000; see also Copin 2000, Copin et al., in preparation). Doing this for the entire sample will provide a statistically reliable determination of the incidence of kinematically decoupled cores, embedded discs and minor axis rotation, and will also provide parametrized input for statistical studies of, for example, the distribution of intrinsic shapes (Franx, Illingworth & de Zeeuw 1991; Bak & Statler 2000) and the construction of dynamical models.

The detailed measurements for individual objects will be compared with fully general galaxy models constructed by means of Schwarzschild's (1979) numerical orbit superposition method (cf. Rix et al. 1997; van der Marel et al. 1998; Cretton et al. 1999). The modelling uses all appropriate imaging and spectral data available, including *HST* and OASIS spectra, to constrain the mass of a central black hole and the orbital structure in the main body of the galaxy. When combined with the constraints on the stellar populations derived from the line-strength distributions (Kuntschner & Davies 1998), this will shed new light on the fundamental connections between the large and small scale dynamics, the formation (and existence) of supermassive black holes in galactic nuclei, and the history of metal enrichment in early-type galaxies.

ACKNOWLEDGMENTS

REFERENCES

Aragón A., Gorgas J., Rego M., 1987, A&A, 185, 97
Arnold R. A., de Zeeuw P. T., Hunter C., 1994, MNRAS, 271, 924
Bacon R. et al., 1995, A&AS, 113, 347
Bacon R., Emsellem E., Copin Y., Monnet G., 2000, in van Breugel W., Bland–Hawthorn J., eds, ASP Conf. Ser. Vol. 195, Imaging the Universe in Three Dimensions. Astron. Soc. Pac., San Francisco, p. 173
Bacon R. et al., 2001, MNRAS, 326, 23 (Paper I)
Bak J., Statler T. S., 2000, AJ, 120, 110
Barbon R., Capaccioli M., Tarenghi M., 1975, A&A, 38, 315
Bender R., 1988, A&A, 202, L5
Bender R., 1990, A&A, 229, 441
Bender R., Nieto J.-L., 1990, A&A, 239, 97
Bender R., Kormendy J., Dehnen W., 1996, ApJ, 464, L123
Bender R., Saglia R. P., Gerhard O. E., 1994, MNRAS, 269, 785
Birkinshaw M., Davies R. L., 1985, ApJ, 291, 32
Bower G. A. et al., 1998, ApJ, 492, L111
Bower G. A. et al., 2001, ApJ, 550, 75
Bresolin F., Kennicutt R. C., Garnett D. R., 1999, ApJ, 510, 104
Bureau M. et al., 2001, in Corsini E. M., Funes J. G., eds, ASP Conf. Ser. Vol. 230, Disk Galaxies and Galaxy Disks. Astron. Soc. Pac., San Francisco, p. 281
Burbidge E. M., Burbidge G. R., 1962, ApJ, 135, 694
Burbidge E. M., Burbidge G. R., Prendergast K. H., 1961, ApJ, 134, 232
del Burgo C., Peletier R. F., Vazdekis A., Arribas S., Mediavilla E., 2001, MNRAS, 321, 227
Busarello G., Capaccioli M., D'Onofrio M., Longo G., Richter G., Zaggia S., 1996, A&A, 314, 32
Buta R., Combes F., 1996, Fund. Cosmic Physics, 17, 95
Byun Y.-I. et al., 1996, AJ, 111, 1889
Caon N., Macchetto F. D., Pastoriza M., 2000, ApJS, 127, 39
Carollo C. M., Danziger I. J., Buson L., 1993, MNRAS, 265, 553
Carollo C. M., Franx M., Illingworth G. D., Forbes D., 1997, ApJ, 481, 710
Chromey F. R., Elmegreen D. M., Mandell A., McDermott J., 1998, AJ, 115, 2331
Copin Y., 2000, PhD thesis, ENS Lyon
Cretton N., de Zeeuw P. T., van der Marel R. P., Rix H-W., 1999, ApJS, 124, 383
Cretton N., Rix H.-W., de Zeeuw P. T., 2000, ApJS, 536, 319
Dalle Ore C., Faber S. M., González J. J., Stoughton R., Burstein D., 1991, ApJ, 366, 38
Davies R. L., Birkinshaw M., 1988, ApJS, 68, 409
Davies R. L., Efstathiou G. P., Fall S. M., Illingworth G. D., Schechter P. L., 1983, ApJ, 266, 41
Davies R. L., Sadler E. M., Peletier R. F., 1993, MNRAS, 262, 650
Davies R. L. et al., 2001, ApJ, 548, L33
Davoust E., Lelievre G., Maury A., Nieto J.-L., 1984, MNRAS, 209, 503
Dressler A., 1980, ApJ, 236, 351
Dressler A., 1984, ApJ, 286, 97
Dressler A., Richstone D. O., 1988, ApJ, 324, 701
Efstathiou G., Gorgas J., 1985, MNRAS, 215, 37P
Efstathiou G., Ellis R. S., Carter D., 1980, MNRAS, 193, 931
Efstathiou G., Ellis R. S., Carter D., 1982, MNRAS, 201, 975
Faber S. M., Jackson R., 1976, ApJ, 204, 668
Faber S. M., Wegner G., Burstein D., Davies R. L., Dressler A., Lynden-Bell D., Terlevich R. J., 1989, ApJS, 69, 763
Faber S. M. et al., 1997, AJ, 114, 1771
Ferrarese L. et al., 2000, ApJ, 539, L9
Fisher D., 1997, AJ, 113, 950
Fisher D., Franx M., Illingworth G. D., 1996, ApJ, 459, 110
Franx M., Illingworth G. D., Heckman T., 1989, ApJ, 344, 613
Franx M., Illingworth G. D., de Zeeuw P. T., 1991, ApJ, 383, 112
Franx M., van Gorkom J. H., de Zeeuw P. T., 1994, ApJ, 436, 642
Garcia A. M., 1993, A&AS, 100, 47
Gebhardt K. et al., 2000a, AJ, 119, 1157
Gebhardt K. et al., 2000b, ApJ, 539, L13

Gerhard O. E., 1993, MNRAS, 265, 213
Geller M. J., Huchra J. P., 1983, ApJS, 52, 61
González J. J., 1993, PhD thesis, Univ. California
Gorgas J., Efstathiou G., Aragon–Salamanca A., 1990, MNRAS, 245, 217
Goudfrooij P., Emsellem E., 1996, A&A, 306, L45
Ho L. C., Filippenko A. V., Sargent W. L. W., 1997, ApJS, 112, 315
Honma M., 1999, ApJ, 516, 693
Hubble E., 1943, ApJ, 97, 112
Huchra J. P., Geller M. J., 1982, ApJ, 257, 423
Jaffe W., Ford H. C., O'Connell R. W., van den Bosch F. C., Ferrarese L., 1994, AJ, 108, 1567
Joseph C. et al., 2001, ApJ, 550, 668
Knapp G. R., Guhathakurta P., Kim D.-W., Jura M. A., 1989, ApJS, 70, 329
Kormendy J., Djorgovski S. G., 1989, ARA&A, 27, 235
Kornreich D. A., Haynes M. P., Lovelace R., 1998, AJ, 116, 2154
Krumm N., Salpeter E. E., 1979, ApJ, 228, 64
Kuntschner H., Davies R. L., 1998, MNRAS, 295, 29
Kuntschner H., Lucey J. R., Smith R. J., Hudson M. J., Davies R. L., 2001, MNRAS, 323, 615
Lauer T. R. et al., 1995, AJ, 110, 2622
Macchetto F. D., Marconi A., Axon D. J., Capetti A., Sparks W., Crane P., 1997, ApJ, 489, 549
Malin D. F., 1984, in Capaccioli M., ed., Proc. IAU Coll. 58, Astronomy with Schmidt Type Telescopes. Reidel, Dordrecht, p. 73
van der Marel R. P., Franx M., 1993, ApJ, 407, 525
van der Marel R. P., Rix H.-W., Carter D., Franx M., White S. D. M., de Zeeuw P. T., 1994, MNRAS, 268, 521
van der Marel R. P., de Zeeuw P. T., Rix H-W., Quinlan G. D., 1997a, Nat, 385, 610
van der Marel R. P., de Zeeuw P. T., Rix H-W., 1997b, ApJ, 488, 119
van der Marel R. P., Cretton N., de Zeeuw P. T., Rix H-W., 1998, ApJ, 493, 613
Martin P., Roy J.-R., 1994, ApJ, 424, 599
Merritt D. R., 1999, PASP, 111, 129
Mould J. R., Akeson R. L., Bothun G. D., Han M., Huchra J. P., Roth J., Schommer R. A., 1993, ApJ, 409, 14
Neistein E., Maoz D., Rix H. W., Tonry J. L., 1999, AJ, 117, 2666
Ochsenbein F., Bauer P., Marcout J., 2000, A&AS, 143, 23
Paturel G. et al., A&AS, 124, 109
Peletier R. F., 1989, PhD thesis, Univ. Groningen
Peletier R. F., Vazdekis A., Arribas S., del Burgo C., Garcia–Lorenzo B., Gutierrez C., Mediavilla E., Prada F., 1999, MNRAS, 310, 863
Pogge R. W., Eskridge P. B., 1993, AJ, 106, 1405
Prugniel P., Zasov A., Busarello G., Simien F., 1997, A&AS, 127, 117
Qian E. E., de Zeeuw P. T., van der Marel R. P., Hunter C., 1995, MNRAS, 274, 602
Rest A., van den Bosch F. C., Jaffe W., Tran H., Tsvetanov Z., Ford H. C., Davies J., Schafer J., 2001, AJ, 121, 2431
Rix H.-W., Zaritsky D., 1995, ApJ, 447, 82
Rix H.-W., de Zeeuw P. T., Cretton N., van der Marel R. P., Carollo C. M., 1997, ApJ, 488, 702
Roberts M. S., Hogg D. E., Bregman J. N., Forman W. R., Jones C., 1991, ApJS, 75, 751
Rots A., 1978, AJ, 83, 219
Sandage A., 1961, The Hubble Atlas of Galaxies. Carnegie Institute of Washington, Washington D.C.
Sarzi M., Rix H.-W., Shields J. C., Rudnick G., Ho L. H., McIntosh D. H., Filippenko A. V., Sargent W. L. W., 2001, ApJ, 550, 65
Schoenmakers R. H. M., Franx M., de Zeeuw P. T., 1997, MNRAS, 292, 349

Schneider S., 1985, ApJ, 288, L33
Schwarzschild M., 1979, ApJ, 232, 236
Statler T. S., 1991, ApJ, 382, L11
Statler T. S., 1994, AJ, 108, 111
Statler T. S., Smecker-Hane T., 1999, AJ, 117, 839
Surma P., Bender R., 1995, A&A, 298, 405
Thronson H. A., Bally J., Hacking P., 1989, AJ, 97, 363
Tonry J. L., 1984, ApJ, 283, L27
Tonry J. L., 1987, ApJ, 322, 632
Tonry J. L., Davis M., 1981, ApJ, 246, 666
Tonry J. L., Dressler A., Blakeslee J. P., Ajhar E. A., Fletcher A. B., Luppino G. A., Metzger M., Moore C. B., 2001, ApJ, 546, 681
Trager S. C., Worthey G., Faber S. M., Burstein D., González J. J., 1998, ApJS, 116, 1
Tully R. B., 1988, Nearby Galaxies Catalogue. Cambridge Univ. Press, Cambridge
Turner E. L., Gott J. R., III, 1976, ApJS, 32, 409
de Vaucouleurs G., Buta R., 1980, AJ, 85, 637
de Vaucouleurs G., de Vaucouleurs A., Corwin H. G., Buta R. J., Paturel G., Fouque P., 1991, Third Reference Catalogue of Bright Galaxies. Springer-Verlag, New York
Vazdekis A., Peletier R. F., Beckman J. E., Casuso E., 1997, ApJS, 111, 203
Wagner S. J., Bender R., Möllenhoff C., 1988, A&A, 195, L5
Wong T., 2000, PhD thesis, Univ. California
Whitmore B. C., Lucas R. A., McElroy D. B., Steiman-Cameron T. Y., Sackett P. D., Olling R. P., 1990, AJ, 100, 1489
Worthey G., 1994, ApJS, 95, 107
Worthey G., Faber S. M., González J. J., Burstein D., 1994, ApJS, 94, 687
Worthey G., Ottaviani D. L., 1997, ApJS, 111, 377
Wozniak H., Friedli D., Martinet L., Martin P., Bratschi P., 1995, A&AS, 111, 115
Wrobel J. M., Heeschen D. S., 1991, AJ, 101, 148
Yahil A., Tammann G. A., Sandage A., 1977, ApJ, 217, 903
de Zeeuw P. T., Franx M., 1991, ARA&A, 29, 239
de Zeeuw P. T., 1996, in Lahav O., Terlevich E., Terlevich R. J., eds, Gravitational Dynamics. Cambridge Univ. Press, Cambridge, p. 1
de Zeeuw P. T., Carollo C. M., 1996, in Bender R., Davies R. L., eds, Proc. IAU Symp. 171, New Light on Galaxy Evolution. Kluwer, Dordrecht, p. 47
de Zeeuw P. T. et al., 2000, ING Newsletter, 2, 11

APPENDIX A: THE SAMPLE

Tables A1 and A2 list the galaxies in the representative sample defined in Section 2.1, for E/S0/Sa galaxies in 'clusters' and in the 'field', respectively. The tables also list a number of global and nuclear properties. In addition to the most common name used in LEDA, we give the Hubble type (NED), numerical morphological type T (LEDA), recession velocity V_{sys} (LEDA), adopted distance modulus Δm (Section 2.1), absolute blue magnitude M_B (Section 2.1), effective $B - V$ colour $(B - V)_e$ (LEDA), central Mg line-strength Mg_2 (Hypercat), effective radius R_e in B (RC3), ellipticity at $\mu_B = 25$ mag arcsec^{-2} ϵ_{25} (LEDA), mean B effective surface brightness μ_e (LEDA), maximum rotation velocity V_{max} (LEDA), central velocity dispersion σ (LEDA), deprojected central cusp slope γ_{phys}^V (Section 2.2), and central black hole mass M_{BH} (Section 2.2).

Table A1. Properties of the 'cluster' galaxies in the representative sample.

Galaxy (1)	Type (2)	T (3)	V_{sys} (4)	Δm (5)	M_B (6)	$(B-V)_e$ (7)	Mg_2 (8)	R_e (9)	ϵ_{25} (10)	μ_e (11)	V_{max} (12)	σ (13)	γ^V_{phys} (14)	M_{BH} (15)
Ellipticals														
NGC3377	E5–6	−4.0	698	30.14	−19.24	0.905	0.278	34	0.39	20.98	89	136	1.15	0.6–2.5(8)
NGC3379	E1	−4.0	877	30.14	−20.16	0.975	0.322	35	0.08	20.72	49	206		0.5–1.6(8)
NGC4278	E1–2	−4.6	612	30.68	−19.93	0.960	0.306	34	0.06	20.97	53	252	0.53	
NGC4374	E1	−3.5	1016	31.06	−21.23	1.000	0.319	51	0.12	20.68	17	297		0.9–2.8(9)
NGC4387	E	−3.4	550	31.06	−18.34	0.965	0.252	16	0.34		57	117	0.72	
NGC4458	E0–1	−3.8	676	31.06	−18.42	0.915	0.233	26	0.06		20	102	1.40	
NGC4473	E5	−4.2	2210	31.06	−20.26	0.990	0.316	26	0.38	20.18	54	191		
NGC4486	E0–1$^+$pec	−4.0	1272	31.06	−21.79	0.980	0.303	95	0.30	21.30	16	351		1.8–3.2(9)
NGC4552	E0–1	−3.4	288	31.06	−20.58	1.000	0.340	29	0.09	20.25	9	264	0.53	
NGC4564	E	−4.1	1116	31.06	−19.39	0.965	0.345	20	0.45	20.43	147	168		4.0–7.0(7)
NGC4621	E5	−4.0	431	31.06	−20.64	0.975	0.293	40	0.24	20.72	120	245		
NGC4660	E	−4.1	1082	31.06	−19.22	0.990	0.306	12	0.21	19.76	149	191		
Lenticulars														
NGC3384	SB0$^-$(s):	−2.6	729	30.14	−19.56	0.955	0.306	25	0.49	19.82		142		0.9–2.5(7)
NGC3489	SAB0$^+$(rs)	−2.1	688	30.14	−19.32	0.845	0.193	20	0.38	19.60	157	138		
NGC4150	S0^0(r)?	−2.4	232	30.68	−18.48	0.830	0.131	18	0.30			148		
NGC4262	SB0$^-$(s)	−2.6	1361	31.06	−18.88	0.970	0.325	13	0.09	20.03	372	186		
NGC4270	S0	−1.1	2349	31.06	−18.28	0.950	0.237	13	0.53	20.79	126	140		
NGC4382	S0$^+$(s)pec	−1.8	745	31.06	−21.28	0.895	0.261	55	0.22	20.74		177		
NGC4459	S0$^+$(r)	−2.0	1182	31.06	−19.99	0.970	0.270	35	0.23	20.99		174		5.9–8.7(7)
NGC4477	SB0(s):?	−1.8	1327	31.06	−19.96	0.970			0.09	21.22		172		
NGC4526	SAB0^0(s):	−1.6	566	31.06	−20.68	0.975	0.304	44	0.63	20.68	136	256		
NGC4546	SB0$^-$(s):	−2.6	1036	31.06	−19.98	0.990		27	0.50	20.36	152	242		
NGC4550	SB0^0:sp	−2.3	407	31.06	−18.83	0.890	0.191	15	0.71		110	80		
NGC4570	S0 sp	−1.7	1731	31.06	−19.54	0.970	0.342	18	0.68	19.93		188		
Spirals														
NGC3623	SABa(rs)	1.0	769	30.14	−20.82	0.975		85	0.76		234	173		
NGC4235	Sa(s)sp	1.1	2332	31.06	−19.20	1.005		27	0.78	21.17	136			
NGC4245	SB0/a(r):	0.4	837	30.68	−18.72	0.920		24	0.17	21.18	161			
NGC4274	(R)SBab(r)	1.4	877	30.68	−20.08	0.980		45	0.63	20.85	218	138		
NGC4293	(R)SB0/a(s)	1.4	823	31.06	−20.37	0.940		83	0.48	22.67	163	163		
NGC4314	SBa(rs)	1.5	957	30.68	−19.55	0.895		34	0.05	21.11	204			
NGC4383	Sa\$ pec	1.1	1663	31.06	−18.93	0.455		11	0.49	19.82	96			
NGC4405	S0/a(rs):	1.3	1751	31.06	−18.54	0.750		−	0.34		68			
NGC4425	SB0$^+$:sp	0.5	1865	31.06	−18.83	0.930		23	0.64	21.28		132		
NGC4596	SB0$^+$(r)	−0.3	1901	31.06	−19.94	0.970		38	0.13	21.28		152		0.4–1.2(8)
NGC4698	Sab(s)	1.4		31.06	−20.05	0.940		33	0.31	21.10	245	172		
NGC4772	Sa(s)	1.2	1042	31.06	−19.56	0.930		24	0.42	20.30	239			

Notes: (1) Galaxy identifier. (2) Hubble type (NED). (3) Numerical morphological type (LEDA). (4) Recession velocity V_{sys} in km s^{-1} (LEDA). (5) Distance modulus Δm in mag, determined as described in Section 2.2. (6) Absolute blue magnitude M_B in mag. (7) Effective $(B-V)_e$ colour in mag (LEDA). (8) Central Mg_2 line strength in mag (Hypercat). (9) Effective radius R_e in the B band, in arcsec (RC3). (10) Ellipticity ϵ_{25} of the contour of 25 mag arcsec^{-2} surface brightness (LEDA). (11) Mean effective surface brightness μ_e in the B band, in mag (LEDA). (12) Maximum observed mean rotation V_{max} in km s^{-1}. For the ellipticals this is the maximum mean stellar rotation of the main galaxy (see Section 2.2). For the lenticulars and the spirals the values taken from LEDA generally refer to the circular velocity. (13) Central velocity dispersion σ in km s^{-1} (LEDA). (14) Average logarithmic slope γ^V_{phys} of the deprojected luminosity profile within 10–50 pc, taken from Carollo et al. (1997, Tables 5 and 8). (15) Reported central black hole mass $M_\odot$, where the notation $a-b(c)$ indicates means $a-b \times 10^c$ $M_\odot$. References given in Section 2.2.

Table A2. Properties of the 'field' galaxies in the representative sample. See text for explanation.

Galaxy (1)	Type (2)	T (3)	V_{sys} (4)	Δm (5)	M_B (6)	$(B-V)_e$ (7)	Mg_2 (8)	R_e (9)	ϵ_{25} (10)	μ_e (11)	V_{max} (12)	σ (13)	γ^V_{phys} (14)	M_{BH} (15)
Ellipticals														
NGC 821	E6?	−4.2	1742	31.86	−20.44	1.020	0.316	50	0.32	22.02	91	208		3.0−7.0(7)
NGC2699	E:	−5.0	1825	31.83	−18.85	0.980	0.282		0.06					
NGC2768	E6:	−3.1	1324	31.66	−21.15	0.960	0.276	64	0.42	21.94	148	188		
NGC2974	E4	−3.6	1983	31.93	−20.32	1.005	0.305	24	0.39	20.74	207	229		
NGC3608	E2	−4.3	1201	30.96	−19.54	1.000	0.329	34	0.21	21.57	26	204	0.80	0.8−2.5(8)
NGC5198	E1−2:	−3.4	2514	32.80	−20.38	0.985	0.322	26	0.14	21.89	4	195		
NGC5813	E1−2	−4.5	1917	32.10	−20.99	1.010	0.319	57	0.24	22.12	8	238	0.24	
NGC5831	E3	−4.3	1660	31.79	−19.73	0.985	0.301	26	0.13	21.48	27	175		
NGC5838	S0−	−3.0	1348	31.36	−19.87	1.010		23	0.59	20.51	225	274		
NGC5845	E:	−4.1	1581	31.69	−18.58	1.120	0.319		0.32	19.84	127	221	0.51	2.5−5.0(8)
NGC5846	E0−1	−4.2	1722	31.98	−21.24	1.030	0.333	63	0.06	21.96	7	250		
NGC5982	E3	−3.9	2876	33.11	−21.46	0.940	0.303	24	0.30	21.08	85	251	0.21	
Lenticulars														
NGC 474	S0⁰(s)	−2.2	2304	32.50	−20.42	0.940		34	0.19	21.99	244	170		
NGC 524	S0⁺(rs)	−1.5	2422	32.58	−21.40	1.070	0.307	50	0.01	21.73		245	0.52	
NGC1023	SB0−(rs)	−2.6	607	30.06	−20.42	1.010	0.311	40	0.56	20.32	138	206	0.74	2.4−4.8(7)
NGC2549	S0⁰(r) sp	−2.0	1064	31.12	−19.36	0.955	0.269	17	0.68	20.05		146		
NGC3414	S0 pec	−2.5	1441	31.52	−19.78	0.930	0.327	21	0.17	20.53	223	246		
NGC2685	(R)SB0⁺pec	−0.7	867	30.79	−19.05	0.935	0.229	32	0.51	21.50	147	99		
NGC2695	SAB0⁰(s)	−2.4	1831	31.83	−19.38	0.930	0.319	16	0.27	20.96		220		
NGC3032	SAB0⁰(r)	−1.7	1561	31.68	−18.77	0.630	0.129	9	0.11	20.01	169	82		
NGC3156	S0:	−2.4	1174	30.90	−18.08	0.770	0.110	14	0.38	20.93	362	84		
NGC5308	S0− sp	−1.1	2029	32.26	−20.27	0.925		18	0.82	19.87	146	260		
NGC7332	S0 pec sp	−1.7	1197	31.42	−19.93	0.905	0.242	15	0.73	19.43	131	134	1.00	
NGC7457	S0−(rs)?	−2.2	758	30.46	−18.81	0.900	0.178	32	0.41	21.57		75		1.7−6.0(6)
Spirals														
NGC1056	Sa:	1.0	1695	31.70	−19.44	1.020			0.44		140			
NGC2273	SBa(r):	0.5	1887	32.17	−20.21	0.940		26	0.25	21.61	228	124		
NGC2844	Sa(r):	0.2	1488	31.66	−18.38	0.810			0.55		145	114		
NGC4220	S0⁺(r)	−0.1	966	30.88	−19.01	0.970		30	0.61	21.36	167	140		
NGC4369	(R)Sa(rs)	1.1	986	31.01	−18.96	0.500		16	0.01	20.41	288			
NGC5448	(R)SABa(r)	1.2	1971	32.36	−20.78	0.760		72	0.48	22.01	207			
NGC5475	Sa sp	1.0	1699	32.06	−19.39				0.74					
NGC5689	SB0⁰(s):	0.4	2147	32.53	−20.32				0.71		170	203		
NGC5953	Sa:pec	−0.4	2061	32.22	−19.61				0.26		120	129		
NGC6501	S0⁺:	−0.3	2958	33.03	−20.38	1.050			0.10		193	222		
NGC7731	(R)SBa:pec	1.2	2866	32.96	−18.78	0.805		15	0.19	21.43	130			
NGC7742	Sb(r)	1.3	1655	31.82	−19.76	0.775		15	0.05	20.23	92	106		

Notes and units as in Table A1.

This paper has been typeset from a TEX/LATEX file prepared by the author.